Probing interfaces and non-centrosymmetry using SHG: a short study guide

Imee Su Martinez*[1,2] and Allen Marbert S. Lee[2]

[1]Institute of Chemistry, University of the Philippines, Diliman, Quezon City, Philippines, 1101
[2]Natural Sciences Research Institute, University of the Philippines, Diliman, Quezon City, Philippines, 1101

ABSTRACT

A primer for second harmonic generation (SHG) spectroscopy as a technique for interfacial analyses is presented in this paper. It includes a systematic discussion of the accompanying theoretical work involved in signal generation, which may serve as an introductory guide for students and researchers. Theoretical derivations of SHG intensity are also presented in this work, to elucidate introduced concepts. The very first working SHG microscope built in the Philippines, is also presented in this paper. In addition, interesting SHG studies on various interfaces through the years are described, including works on semiconductors, nanomaterials, lipid membranes, and biological samples.

INTRODUCTION

Interfaces as key regions in space where phases meet and reactions begin, define the need to perform interfacial studies. Techniques such as SHG spectroscopy or microscopy are needed to be able to characterize interfaces, distinct and independent from that of the bulk. They are particularly important in systems, where interfacial phenomena play a vital role such as in nanomaterials, semiconductors, adsorbents, and catalysts. The higher the surface area to bulk volume ratio, the more emphasized the interfacial effects, and the greater the need to be able to characterize and understand associated interfacial processes. Since interfaces are ubiquitous, surface-specific techniques are highly useful.

Interfaces are defined as monolayers of material situated along the boundary between two macroscopic phases (Myers 1999; Berg 2009). The terms ‘interface’ and ‘surface’ are not interchangeable, although they are similar (Somorjai 1994). The former describes all types of boundaries, and is the more appropriate term when discussing phase boundary properties and mechanisms, while the latter only describes boundaries between a condensed phase and a gaseous phase or vacuum.

Interfaces have finite thickness ranging from a few Angstroms to tens of nanometers (Somorjai 1994; Somorjai and Li 2010). They are inhomogeneous, ubiquitous, and their properties differ greatly from their bulk material. This difference can be explained by two major factors – chemical composition and molecular orientation. The chemical composition of an interface is more complex compared to the bulk. The components of the bulk materials may or may not exist at the interface at any given point in time (Berg 2009). In terms of geometric arrangement, the molecules at the interface are asymmetric. This is due to the combination of intermolecular forces experienced by the interface. Consequently, this creates a break in the region of space occupied by the interface making it non-centrosymmetric (Eisenthal 1996). Molecules at the surface therefore experience an anisotropic environment.

There are five major types of interfaces – solid-gas, solid-liquid, solid-solid, liquid-liquid, and liquid-gas interfaces (Somorjai 1994). Gas-gas interfaces do not exist since gases can completely mix with one another (Berg 2009). The first three

*Corresponding author
Email Address: ismartinez@up.edu.ph
Date received: August 11, 2023
Date revised: December 5, 2023
Date accepted: January 12, 2024
DOI: https://doi.org/10.54645/2024171TRN-31

KEYWORDS

SHG, NLO, interfaces, surfaces, chemistry

types mentioned are also classified as solid interfaces. Common techniques used for solid interfacial studies include Auger electron spectroscopy (AES), soft x-ray photoemission, ion-scattering spectroscopy, and secondary-ion mass spectroscopy (SIMS) (Gaarenstroom 1981; Lee et al. 1994; Young and Hoflund 1988; Mahoney et al. 2010; Benninghoven 1969). All these methods utilize the fact that solid interfacial analyses are dependent on the way the interface was prepared (Berg 2009). The last two types belong to the fluid interfaces. Compared to solid interfaces, interfaces between fluid phases are more difficult to analyze. Analyzing them using more traditional spectroscopic methods such as UV-VIS absorption and Raman spectroscopy is not possible, because these are not capable of bulk and interfacial differentiation (Eisenthal 1996). Non-linear optical spectroscopy such as SHG and sum frequency generation (SFG) are the more appropriate techniques. These techniques are capable of selectively probing interfaces, since second-order processes are forbidden in the bulk. Thus, systems like bulk liquids, gases, amorphous, and centrosymmetric crystalline solids cannot generate second harmonic (SH) and sum frequency signals (Eisenthal 1996; Shen 1989). There are other minor types of interfaces, which are commonly used in theoretical derivations and high vacuum processes. These are called vacuum interfaces (Myers 1999).

SHG spectroscopy is a widely used method for analyzing interfaces. It is generated from the non-linear interaction of light and matter. Unlike SFG spectroscopy, which is an analogous technique, SHG involves equivalent incoming frequencies (ω) (Shen 1989). SH signals can be used to determine properties of molecules at the interface such as orientation and symmetry. It can also be used to characterize non-centrosymmetric bulk materials such as crystals, however, it does not provide molecular vibrational information like SFG (Lüpke 1999; Ok et al. 2006). Currently, SHG thrives in applications related to interfacial imaging, such as adsorption studies, molecular chirality, and biological samples (Campagnola and Loew 2003; Cox et al. 2003; Eckenrode et al. 2005; Petralli-Mallow et al. 1993). Environmental chemistry studies such as antibiotic adsorption between water and mineral oxide interfaces, and heavy metal adsorption on silica interfaces are also being done, providing an alternate perspective on different environmental processes, whether naturally-occurring or anthropogenic (Mifflin et al. 2006; Geiger 2009; Mifflin et al. 2005; Konek et al. 2008).

The main objective of this work is to introduce SHG spectroscopy as a technique for analyzing interfaces and surfaces. This educational guide will aid in learning basic concepts pertaining to this technique, and in explaining observed phenomenon during experiments. The flow of concepts presented in this paper is designed to aid researchers acquire a more organized approach in understanding the theory behind SHG. Actual calculations to derive SHG intensity are shown, to serve as an example on the application of presented concepts. A brief discussion on the theory of SHG, the development of the technique through the years, as well as its uses, are discussed in this paper.

STUDY GUIDE

1. Introduction to second-order non-linear spectroscopy

Non-linear optical processes refer to the non-linear response of materials to light (Boyd 2008). Depending on the degree of the resulting induced polarization generated from this interaction, the process can be second order, third order, and so on. Materials, which are non-centrosymmetric tend to generate a second order non-linear response. Most optical materials respond in a non-linear manner, and the assumption of linearity is used primarily for the approximation and simplification of real systems (New 2011). In fact, the intensity of light striking a particular sample dictates whether non-linear responses are significant.

If a low-intensity ambient light beam interacts with a sample, the resulting induced electric dipole (μ) due to the incoming electric field (E) is expressed as the sum of the permanent electric dipole (μ_0) and the resulting dipole contribution, which is dictated by the polarizability (α) of the electrons of the material (Lambert et al. 2005). This is expressed in Equation 1 below.

$$\mu = \mu_0 + \alpha E \qquad (1)$$

Consequently, the resulting polarization or induced dipole moment per unit volume experienced by a system can be represented using Equation 2.

$$P = \varepsilon_o \chi^{(1)} E; \qquad (2)$$

where P denotes the bulk polarization, ε_o is the vacuum permittivity, and $\chi^{(1)}$ is the first-order susceptibility, or simply linear susceptibility. In a first order response, the energy coming from the incident light is relatively low, such that susceptibilities coming from higher-order polarization may be neglected. Examples of linear optical phenomena are transmission and absorption, which are the known processes in UV-VIS, IR, or Raman spectroscopies (Perkampus 1992).

However, if the energy of the incoming light beam is strong enough, the expressions for linear events given in Equations 1 and 2 become incomplete due to contributions from non-linear or higher order susceptibilities. These higher-order polarizations are then considered, as described by higher order hyperpolarizabilities shown in Equation 3.

$$\mu = \mu_0 + \alpha E + \beta E^2 + \gamma E^3 + \ldots; \qquad (3)$$

where α, β, and γ represent the first, second, and third order hyperpolarizability coefficients, respectively. Polarization generated on the medium can then be expressed as Equation 4, where $\chi^{(2)}$ and $\chi^{(3)}$ are the higher-order non-linear susceptibilities (Boyd 2008; Lambert et al. 2005).

$$P = \varepsilon_0\left[(P^{(1)} = \chi^{(1)}E) + (P^{(2)} = \chi^{(2)}E^2) + (P^{(3)} = \chi^{(3)}E^3) + \ldots\right] \qquad (4)$$

$\chi^{(i=1,2,3\ldots)}$ relates the degree of polarization response to the electric field intensity, which is the macroscopic non-linear susceptibility. For contributions beyond the linear contribution, i=2, 3, and so forth. On the other hand, hyperpolarizability is described as molecular level polarizability (Rao et al. 2003).

The expressions for non-linearity given in Equation 3 and Equation 4 require that the applied electromagnetic field from the incident light is comparable to the electromagnetic field coming from the electrons of the medium – a condition only possible for high intensity light sources such as lasers (New 2011). This is the reason why the history of non-linear optics (NLO) is very much intertwined with the history of the laser. In fact, NLO progressed significantly after the invention of the ruby pulsed maser in 1960, which generated monochromatic light beams with electric fields of the order 10^5 V/cm (Franken et al. 1961; Maiman 1960; Collins et al. 1960).

The equations discussed above work under two assumptions (Lambert et al. 2005; Peterson et al. 2011). The first assumption explains that all calculations and derivations must follow the Born-Oppenheimer approximation, wherein the electric field coming from the incident light interacts only with the electrons. The second assumes that contributions from optical magnetic fields and electric multipoles are neglected. Only the dipole induced by the macroscopic electric field will be considered, and additional effects coming from neighboring induced dipole are ignored.

2. Second harmonic generation spectroscopy

SHG is a second-order non-linear process resulting from the interaction of two photons of the same frequency (ω) undergoing temporal and spatial overlap (Shen 1989). This generates a beam of light with a frequency ($\omega' = 2\omega$) twice that of the original incoming frequency. The energy diagram describing SHG is shown in Figure 1. A ground state energy level photon effectively combines with a second photon upon interaction with matter. The combined photons will then reach a higher energy level called virtual state, carrying a frequency twice the original, which subsequently goes back to ground state. The entire process occurs in a single quantum mechanical event; thus, the higher energy state is simply called virtual state. Theoretically, the energy carried by the photons is conserved during combination (New 2011).

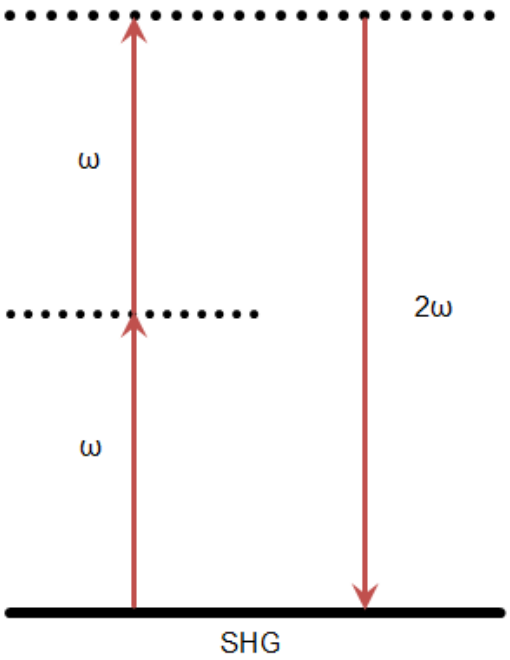

Figure 1: SHG energy diagram.

To generate SHG, conservation of energy and linear momentum needs to be achieved. Equations 5 and 6 describe these requirements, where equation 5 shows how the incoming and the SH beam propagates at an angle perpendicular to the plane along the positive z direction. This is the non-linear form of Snell's law. Equation 6 on the other hand, indicates the phase matching condition, where the maximum phase matching is achieved when $\Delta k = 0$ (Bloembergen and Pershan 1962). Figure 2 shows a sample SHG optical set-up. This depicts a widely accepted phenomenological model purported by Heinz, Guyot-Sionnest, and Shen back in the 1980s (Shen 1989; Heinz 1982; Guyot-Sionnest et al. 1986). This geometry is identified as a single beam co-propagating geometry, producing reflection and transmission SH beams propagating at the xz-plane. θ is the angle of incidence of the incoming light from the z-axis or the surface normal, while θ′ is the angle of the SH beam. n is the refractive index of the medium, where the fundamental beam propagates, and n′is the refractive index of the medium at which the SH beam propagates. $k_{\omega,z}$ and $k_{\omega',z}$ are the wave vectors of the fundamental light and the SH light, respectively. The bulk linear dielectric responses of the two media, which are in contact, are designated as ε_1 for medium 1, and ε_2 for medium 2. The interfacial dielectric response is in turn denoted as ε'.

$$n'\omega'\sin\theta' = n(2\omega)\sin\theta \qquad (5)$$

$$\Delta k = 2k_{\omega,z} - k_{\omega',z} \qquad (6)$$

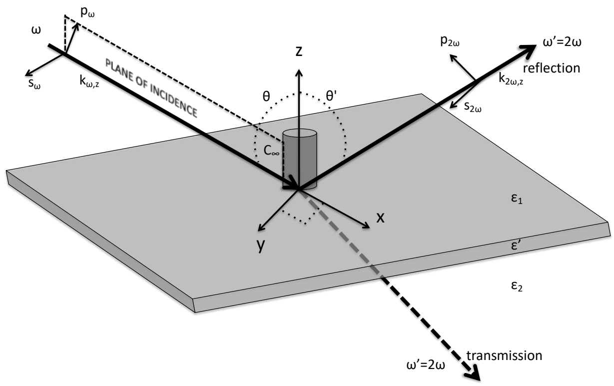

Figure 2: Single beam SHG set-up.

In this model, the electric fields produced at the interfacial region with a dielectric constant ε' is related to the non-linear surface polarization or the polarization sheet. The assumption is that the interfacial layer is very much thinner compared to the wavelength of the fundamental beam.

When a plane wave radiation is assumed for each pump beam in a medium (m), whether medium 1 or 2 as depicted in Figure 2, the electric field can be expressed in terms of Equation 7. $E_m(\omega)$ is the amplitude of the electric field described by the polarization vector $\hat{e}(\omega)$, and k_m is the wave vector for the propagating radiation along the xz-plane. Following the Euler formula, Equation 8 with the frequency (ω) and time (t) dependent expression is also used to describe an electric field (E) in medium 1 (Boyd 2008; Heinz 1991).

$$E_m(x,y,z,t) = E_m(\omega)\exp^{i\,k_m\cdot x - i\omega t} + c.c. = E_m(\omega)\hat{e}(\omega)\exp^{i\,k_m\cdot x - i\omega t} + c.c. \qquad (7)$$

$$E = E_1\cos(\omega t) \qquad (8)$$

Substituting Equation 8 into the expression for induced polarization P from Equation 4 for any fundamental frequency (ω) will lead to Equation 9. The second term in the equation shows that the electric field due to induced polarization, has a frequency twice as much as the original. This is the mathematical description of SHG, which when taken out of the overall polarization equation is expressed as Equation 10. $e(\omega)$ is related to the polarization vector $\hat{e}(\omega)$, through the Fresnel factor F_{1-2} shown in equation 11 (Boyd 2008). Also, the description for the third harmonic generation can be observed in the third term of Equation 9.

$$P = \varepsilon_0\left[\chi^{(1)}E_1\cos\omega t + \chi^{(2)}\frac{E_1^2}{2}(1+\cos 2\omega t) + \chi^{(3)}\frac{E_1^3}{4}(3\cos\omega t + \cos 3\omega t) + \ldots\right] \quad (9)$$

$$P^{(2)}(2\omega) = \chi^{(2)}\!:\mathbf{E}(\omega)\mathbf{E}(\omega) = \chi^{(2)}\!:e(\omega)e(\omega)E(\omega)E(\omega) \quad (10)$$

$$e(\omega) = F_{1-2}\hat{e}_i(\omega) \quad (11)$$

DISCUSSION

The Fresnel factor (F_{1-2}) describes how the electric field propagates from one medium to another, such as from air to an interface. They are dependent on the refractive index of matter at which the light beam propagates. An incoming electric field in medium 1, described as $E_1(\omega)\hat{e}_1(\omega)$ reaches the interface generating a surface electric field of $E_1(\omega)F_{1-2}\hat{e}_1(\omega)$. F_{1-2} relates the incoming electric field to that of the generated electric field on the surface and determines the extent of how a beam is transmitted or reflected. In an isotropic media, the Fresnel factor is a summation of its three diagonal elements shown in Equation 12 (Heinz 1991).

$$F_{1-2} = F_{1-2}^{xx}\,\hat{x}\hat{x} + F_{1-2}^{yy}\,\hat{y}\hat{y} + F_{1-2}^{zz}\,\hat{z}\hat{z} \quad (12)$$

The resulting intensity I(2ω) of a SH beam is proportional to the square modulus of the induced polarization on the surface shown in Equation 13 (Shen 1989).

$$\mathrm{I}(2\omega) \propto \left|\mathrm{P}^{(2)}(2\omega)\right|^2 \quad (13)$$

The longer form of the equation for SHG intensity given the optical set-up in Figure 2 is shown in Equations 14 and 15. I(ω) is the intensity of the fundamental beam, c is the speed of light, $\mathbf{E}(2\omega)$ is the electric field of the SH, and A is the area of illumination of the fundamental beam. In addition, $\mathrm{P}^{(2)}(2\omega)$ is the induced polarization from matter, which generates $\mathbf{E}(2\omega)$, while $\chi_{\mathrm{eff}}^{(2)}$ is the effective second order non-linear susceptibility tensor at the interface.

$$\mathrm{I}(2\omega) = \frac{16\,\pi^3(\omega)^2}{c^3[\boldsymbol{E}(2\omega)E(\omega)E(\omega)]^{1/2}} sec^2\theta\left|e(2\omega)\cdot\chi^{(2)}\colon e(\omega)e(\omega)\right|^2 \mathrm{I}(\omega)^2 \quad (14)$$

$$\mathrm{I}(2\omega) = \frac{32\,\pi^3}{Ac^3} sec^2\theta\left|\chi_{eff}^{(2)}\right|^2 \mathrm{I}(\omega)^2 \quad (15)$$

Non-linear Fresnel factors are represented as $L_{x,y,z}$ to differentiate them from the general representation F_{1-2}. The subscripts pertain to the Cartesian coordinates or coordinates of the laboratory. $L_{x,y,z}$ relates the induced polarization to the emitted electric field within the context of phase-matching condition. Specific Fresnel equations have been derived for various beam geometries through the years such as the work of Sipe, Conboy, and Wang for co-propagating and counter-propagating geometries. (Sipe et al. 1987; Kriech and Conboy 2004; Wang et al. 2005).

Given the co-propagating optical geometry in Figure 2, the nonlinear Fresnel factors can be derived. Equation 16-18 shows the Fresnel equations derived by Wang and co-workers given that the thickness of the interface is insignificant compared to the wavelength of the fundamental beam (Collins et al. 1960).

$$L_{xx}(\omega_i) = \frac{2\sqrt{\varepsilon_2(\omega_i) - \varepsilon_1(\omega_i)sin^2\theta}}{\sqrt{\varepsilon_2(\omega_i) - \varepsilon_1(\omega_i)sin^2\theta} + \frac{\varepsilon_2(\omega_i)}{\sqrt{\varepsilon_1(\omega_i)}}cos\,\theta} \quad (16)$$

$$L_{yy}(\omega_i) = \frac{2\sqrt{\varepsilon_1(\omega_i)}\ cos\,\theta}{\sqrt{\varepsilon_2(\omega_i) - \varepsilon_1(\omega_i)sin^2\theta + \frac{\varepsilon_2(\omega_i)}{\sqrt{\varepsilon_1(\omega_i)}}cos\,\theta}} \quad (17)$$

$$L_{zz}(\omega_i) = \frac{\frac{2\varepsilon_2(\omega_i)\sqrt{\varepsilon_1(\omega_i)}}{\varepsilon'(\omega_i)}cos\,\theta}{\sqrt{\varepsilon_2(\omega_i) - \varepsilon_1(\omega_i)sin^2\theta} + \frac{\varepsilon_2(\omega_i)}{\sqrt{\varepsilon_1(\omega_i)}}cos\,\theta} \quad (18)$$

The major requirement for a system to be SHG active is non-centrosymmetry (Heinz 1982; Goldacker et al. 1999; Boyd 2020). This refers to systems that do not contain inversion symmetries. Non-centrosymmetry allows these materials to generate induced dipole moments that lead to macroscopic, non-linear polarization. SHG signals are therefore impossible to generate in the bulk where molecules are randomly arranged, making the process highly applicable to interfaces. An exception, however, are crystals or ordered structures having the required symmetry, which can produce second-order non-linear signals coming from the bulk.

Describing the relationship of the incoming electric fields to the outgoing field due to the induced polarization on the surface is $\chi^{(2)}$ or the second-order susceptibility. $\chi^{(2)}$ is a third-rank tensor with 27 unique components because of its dependency to the 3 Cartesian axes (Lambert et al. 2005). It contains information regarding molecular orientation and symmetry. In SHG, the elements of $\chi^{(2)}$ may be reduced from 27 (Equation 19) to 4 (Equation 20) non-zero independent elements depending on the (a) symmetry of the molecules at the surface, (b) beam geometry with respect to the surface normal, and (c) polarization combination of the incoming and outgoing beams, considering of course that Neumann's Principle and Kleinman symmetry are in effect (Lambert et al. 2005; Byers et al. 1994). The surface molecules are normally assumed to have a $C_{\infty v}$ symmetry, which becomes C_∞ if they are chiral molecules. Also in an isotropic surface, the axes pertaining to x and y are equivalent, leading to the elimination of terms. In Equation 20, χ_1, χ_2, and χ_3 pertain to the achiral contribution to the SHG signal, while χ_4 is the chiral contribution.

$$\chi_{ijk}^{(2)} = \begin{bmatrix} \chi_{xxx}^{(2)} & \chi_{xyx}^{(2)} & \chi_{xzx}^{(2)} & \chi_{yxx}^{(2)} & \chi_{yyx}^{(2)} & \chi_{yzx}^{(2)} & \chi_{zxx}^{(2)} & \chi_{zyx}^{(2)} & \chi_{zzx}^{(2)} \\ \chi_{xxy}^{(2)} & \chi_{xyy}^{(2)} & \chi_{xzy}^{(2)} & \chi_{yxy}^{(2)} & \chi_{yyy}^{(2)} & \chi_{yzy}^{(2)} & \chi_{zxy}^{(2)} & \chi_{zyy}^{(2)} & \chi_{zzy}^{(2)} \\ \chi_{xxz}^{(2)} & \chi_{xyz}^{(2)} & \chi_{xzz}^{(2)} & \chi_{yxz}^{(2)} & \chi_{yyz}^{(2)} & \chi_{yzz}^{(2)} & \chi_{zxz}^{(2)} & \chi_{zyz}^{(2)} & \chi_{zzz}^{(2)} \end{bmatrix} \quad (19)$$

$$\chi_{ijk}^{(2)} = \begin{bmatrix} \chi_1 = \chi_{zzz}^{(2)}, \chi_2 = \chi_{zxx}^{(2)} = \chi_{zyy}^{(2)}, \\ \chi_3 = \chi_{xzx}^{(2)} = \chi_{yzy}^{(2)} = \chi_{xxz}^{(2)} = \chi_{yyz}^{(2)}, \\ \chi_4 = \chi_{xyz}^{(2)} = -\chi_{yxz}^{(2)} = \chi_{xzy}^{(2)} = -\chi_{yzx}^{(2)} \end{bmatrix} \quad (20)$$

In fact, depending on the beam geometry, whether co-propagating (Figure 3A,B) or counter-propagating (Figure 3C,D), and the polarization combination assigned, the achiral and chiral contributions can be separated from each other (Kriech and Conboy 2005). This was shown in the work of Kriech and Conboy where the chiral $\chi_{xyz}^{(2)}$ contribution was fully separated from the achiral $\chi_{yzy}^{(2)}$ (Kriech and Conboy 2004). The optical set-up was counter-propagating similar to Figure 3D with incoming beams set to varying polarization angles from s to p polarization, and the outgoing beam transmitted along the z-direction set to x and y polarization. In terms of the molecular level hyperpolarizabilities $\beta_{ijk}^{(2)}$, the dependence of $\chi_{ijk}^{(2)}$ is expressed in terms of Equation 21 (Kriech and Conboy 2004). N here is the number of molecules, and the brackets signify an average over all possible molecular orientations.

$$\chi_{ijk}^{(2)} = N\,\langle\beta_{ijk}^{(2)}\rangle \quad (21)$$

S-polarized light per convention is perpendicular with respect to the plane of incidence as shown in Figure 1, while p-polarized light is parallel. S-polarization can therefore be resolved into one axis, in this case the y-axis, while p-polarization can be resolved into two axes, the x and the z. When the transmitted beam is along z, the s and p polarizations become y and x, respectively.

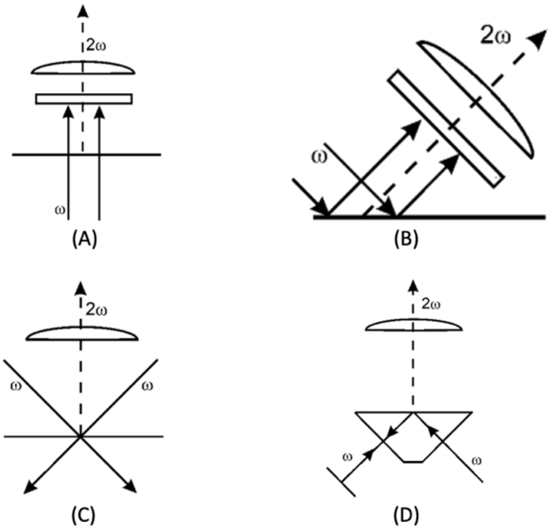

Figure 3: Different geometries applicable for SH analysis: (A) collinear, (B) copropagating, (C) counter-propagating, (D) counter-propagating with prism (Flörsheimer 1999). The detectors are located along the propagation direction of the SHG beam.

The earliest and the simplest geometry proposed by Flörsheimer's group is the collinear configuration depicted in Figure 3A (Flörsheimer 1999). This configuration allows wide area coverage for analysis and is highly applicable using stigmatic spectroscopes and microscopes (Peterson et al. 2011; Marrucci et al. 2002). However, this design presented several errors caused by excessive light and reflection. In response to this disadvantage, Schulz and Seebauer proposed a non-collinear configuration with the beams co-propagating from the same direction (Figure 3B) that will not only resolve the problem of reflection, but is capable of tensor element determination (Schultz et al. 1993). This geometry however, can only obtain high magnification and high resolution images from a small area of the object field – a contrast to the previous geometry (Cheng et al. 2020). Flörsheimer's group developed another design (Figure 3C) to minimize the disadvantages of the two previous configurations (Flörsheimer 1999). The design is based on a non-collinear geometry utilizing counter-propagating beams. The images obtained from this geometry gave better resolution and magnification. Further improvements were constantly being proposed like the configuration given in Figure 3D. In this design, the incoming light beam strikes a prism allowing separation of the excess light and the SHG signal. This design offers additional two advantages, which are enhancement of beam energies and harmonic conversion efficiency. The efficiency of a configuration is measured by the harmonic conversion efficiency (**η**) shown in Equation 22.

$$\eta = \frac{I^{(2\omega)}}{I^{(\omega)}} \qquad (22)$$

The higher the value obtained for η, the better the spectrum and image resolution (Flörsheimer 1999). Other parameters considered for geometry optimization includes the angle of incidence, critical angle for total reflection, intensity of the laser beam, and the number of laser pulses per second.

Given a set-up with co-propagating geometry, calculated SHG intensities performed by the group using Wolfram Mathematica is shown in Figure 4. The wavelength of the fundamental beam used was 1064 nm, and the phase matching angle was set to θ = 22.8656°. The refractive indices used were based on the values possessed by a beta barium borate (b-BBO) negative uniaxial non-linear crystal with an ordinary refractive index of n_o= 1.6651 and extraordinary refractive index of n_e= 1.5425 at 1064 nm, as well as n_o= 1.6749 and n_e= 1.5555 at 532 nm. The incidence refractive index is at n_I= 1.00. The incoming beam polarization is set to s-polarization, while the outgoing SHG beam is at varying polarization angles Ω. Different point group symmetries were also tried for the calculation exercise.

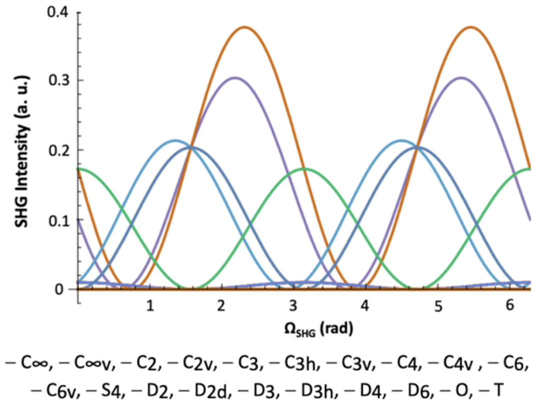

Figure 4: Calculated SHG intensities at varying output polarization angles.

SHG STUDIES OF VARIOUS SAMPLES

Since the 1960's, SHG has proven itself valuable in characterizing various samples, especially interfaces. Through the years, several very interesting studies were performed using this technique. In this section, SHG studies were discussed to demonstrate the usefulness of SHG, showing its history and some chosen recently published works.

1. Crystals and Glass Materials

The earliest samples characterized using SHG are non-centrosymmetric materials possessing dielectric coefficients high enough to generate SHG signal. These are quartz crystal, glass-type materials, and non-linear optical crystals. Table 1 shows SHG studies involving these materials.

Table 1: SHG Studies on crystals and glass materials.

Sample	Summary
Quartz crystals (Franken et al. 1961)	SHG was first observed.
Quartz and potassium dihydrogen phosphate (KH_2PO_4 or KDP) crystals (Kleinman 1962)	These experiments are based upon the theory behind SHG, focusing on the effect of anisotropy.
Lithium niobate, lithium tantalate, and potassium titanyl phosphate (KTP) (Driscoll et al. 1986)	These crystals, which are called quasi-phase matching (QPM), requires periodic modulation of the non-linear optical coefficient to achieve phase matching.
Beta barium borate (β-BaB_2O_4 or BBO), lithium triborate (LiB_3O_5 or LBO), and KDP crystals (Eckardt 2005)	These crystals are considered to be efficient SHG generators due to their birefringent phase matching (BPM) capabilities.
$KBe_2BO_3F_2$ (KBBF) crystal (Chen et al. 2005)	This layered crystal is able to achieve BPM at 386-193 nm., while typical borate NLO crystals cannot. However, the efficiency is quite low due to difficulties in growing these crystals to result in optimum signal generation.

Twin-controlled crystalline quartz structure (Kurimura et al. 2011)	To mark the 50th year anniversary of non-linear optics, the authors achieved the shortest SHG emission at 193 nm for a QPM material.
Deep UV (DUV) harmonic crystals (Halasyamani and Rondinelli 2018)	These crystals were able to achieve coherent emission at 177.3 nm.
Ternary glass system (90–x) GeO_2–$10Na_2O$–xTa_2O5 (Poirier et al. 2019)	A $\chi^{(2)}$ response of 0.06-0.3 pm/V was obtained depending on the glass composition and poling conditions, showing that sodium depletion led to enhanced network structure through oxide bond formation of Ta and Ge.
Silica glass microstructured optical fiber (MOF) infiltrated with 2-methyl-4-nitroaniline (Violakis et al. 2020)	The authors used different poling conditions such as applied temperature and electric fields on the sample. Enhanced crystallinity through poling improved SHG efficiency and transmission of the 1064 nm fundamental beam.
HgI_2–Ga_2S3–Ge_2S_2 (Tverjanovich et al. 2020)	Isotropic homogeneous glass Ga–Ge–S in the presence of HgI_2 molecules became SHG active, such that the intensity of generated SH varied with the amounts of embedded HgI_2. The enhancement in SHG efficiency is comparable to that of a well-known NLO crystal, LBO.
Sm_2O_3-doped sodium borophosphate niobium (SmBPN) glasses (He et al. 2021)	Laser induced thermal poling (LITP) was used to create SHG micropattern on the glass. The method proved to be successful in creating accurate micropattern design of second order optical material.
Water-resistant titanium iodate crystals (Fang et al. 2021)	Non-centrosymmetric (NCS) crystals for high performance SHG are the trend these days. The crystal in this study exhibited good SH conversion at the visible and mid-IR region.
Borate crystals (Chen et al. 2021)	Aliovalent substitution are also being performed involving site-to site atomic displacement at the structural level such as cation replacement, or the addition of anions, which led to SHG enhancement in the traditional borate crystals.

2. Solid Surfaces

SHG studies on crystal bulk materials led to several ground-breaking work in the characterization of interfaces, particularly adsorbed monolayers of molecules on solid surfaces. The development of the Nd:YAG laser and ultrashort pulse lasers , which are able to provide enough energy to generate second order processes in these types of samples significantly propelled advancement in surface characterization (Shen 1989). SHG generated from centrosymmetric media such as metals and semiconductors were observed but are limited to the surface of the materials. SHG studies involving these surfaces are shown in Table 2.

Table 2: SHG Studies on solid surfaces.

Sample	Summary
Thin slab of nonlinear material (computational) (Bloembergen and Pershan 1962)	The phenomenological scheme behind surface and interfacial SHG of dielectrics was elucidated under reflection mode.
Silver mirror surfaces (Brown et al. 1965)	The very first experimental demonstration of SHG from interfaces of materials.
Silver surface (Brown and Matsuoka 1969)	Effect of adsorption on metal surfaces on SHG was first elucidated where it was observed that the presence of contaminants on the Ag surface considerably changed the SHG signal.
Rh(111) crystal surface (Tom et al. 1984)	SHG was used to study adsorption of O_2, CO, and Na on the crystal surface
Ni(111) surface (Zhu et al. 1988)	Diffraction of SHG signal was used to study surface diffusion of CO.
Ni(111) surface (Anderson and Hamilton 1988)	Local site symmetry was shown to greatly affect SH generation. Adsorption of hydrogen on the surface resulted in a decrease in SH intensity, even though symmetry about the surface normal was retained.
Pd(111) surface (Hamilton et al. 1990)	SHG as a function of exciting wavelength, azimuthal sample orientation, and exposure to hydrogen and CO was performed. A tenfold increase in SH intensity was observed for hydrogen adsorption, but not for CO adsorption
Ni(110) surface (Zhu et al. 1991)	SHG second order non-linear susceptibility was investigated as CO coverage was varied.
Cu(111) electrode surface (Bradley et al. 1991)	SHG studies show the existence of surface oxides even in ultra-high vacuum.
Gold surface (Buck et al. 1992)	SHG was used to study the adsorption kinetics of n-alkyl thiols.
Chromophoric self-assembled monolayers (SAM) on Si(111) substrate (Zhou et al. 1997)	SH intensity in this system was found to be dependent on the thickness of the oxide layer.

Monolayers (computational) (Simpson and Rowlen 1999)	Simulation of monolayer orientation studies using SHG.
Azobenzene-functionalized SAMs (Schulze et al. 2015)	SHG was used to determine the NLO properties of the photoswitching SAM in its different states.
Polystyrene surface (Cole et al. 2019)	Elucidation of pollutant adsorption using angle resolved SHG scattering.
Graphene surface (Tokman et al. 2019)	Here, fundamental beam variation on SHG signal was performed to investigate the surface of a 2D material.
Graphene surface (Yang et al. 2020)	SHG was shown to be a potential metrology tool through the structural modification of graphene such as bilayer twisting.
Sr_2IrO_4 (Seyler et al. 2020)	Anomalous SHG signal coming from the sample was attributed to surface-magnetization induced processes that is enhanced by strong spin orbit. Hidden order within the structure, and the presence of layered square lattice iridate, were thought to contribute to the generated SH signal.
$[(C_2H_4OH)C_4H_9NS]CdCl_3$ polymer (Wang et al. 2021)	SHG was used to monitor the adsorption of Pd(II) to the polymer's thioether groups.
Graphene surface (C. Zhang et al. 2021)	SHG signal enhancement through graphene doping.
$MoSi_2N_4$ 2D semiconductor (Kang and Lin 2021)	SHG was shown to be dependent on the structural details of the semiconductor
MoS_2 and WS_2 on fluorine tin oxide (FTO) (Vianna et al. 2021)	Monolayers of transition metal dichalcogenides or TMDCs show high SH generating capability.
SnP_2Se_6 with SiN photonic platform (Zhu et al. 2023)	Electronic-photonic integrated circuits (EPICs) from 2D semiconductor materials such as this sample exhibit efficient on-chip SHG modulation and telecom band photodetection that are reliant on wavelength up conversion.

3. Solid-liquid Interfaces

One of the earliest SHG studies on solid-liquid interfaces, and the most common are electrode-electrolyte interfaces. This is because chemisorption and changes on the electrode surface result in significant SHG signal difference due to surface electron density variation. Depending on the type of atoms or molecules that attach to the electrode, and how they affect electrode surface structure, the resulting generated signal varies. This makes SHG an ideal tool for the in-situ monitoring of these types of interfaces. Table 3 lists SHG studies investigating these interfaces.

Table 3: SHG Studies on solid-liquid interfaces.

Sample	Summary
Silver (Chen et al. 1981)	SHG was used to detect monolayer adsorption of pyridine and AgCl on silver through an electrolytic process. This was one of the earliest works performed on solid-liquid interfaces.
Silver electrode (Bradley et al. 1991; Richmond et al. 1987; Shannon et al. 1987; Georgiadis and Richmond 1991; Campbell and Corn 1987; Campbell et al. 1990; Corn and Higgins 1994)	One of the earliest studies of using SHG in tandem with electrochemistry to detect chemisorption on silver electrodes.
Iron electrode (Biwer et al. 1986)	SHG was used to investigate the formation of films on the electrode surface under different solutions and potentials.
Iron electrode (Schauer et al. 1989)	Angle of incidence and polarization studies were performed to investigate the structural information on the oxide layer on the electrode surface.
Nickel electrode (Biwer et al. 1989)	SHG was used as a tool to monitor corrosion in the electrode immersed in 0.1 M NaOH. Two laser sources were used to differentiate between charging and compositional effects on the SHG signal
Nickel electrode (Frye et al. 1990)	Changes in SHG intensity was observed as passive films were formed on the electrode surface.
Water-silica interfaces (Ong et al. 1992)	SH signal was generated from polarized water molecules.
TiO_2 electrode (Lantz and Corn 1994)	SHG was used to investigate the surface electrostatic fields variation of the electrode.
Steel (Klenerman et al. 1994)	The kinetics of adsorption and chemisorption of compounds used for corrosion prevention was monitored using SHG.
Malachite green molecules adsorbed on microspheres (Wang et al. 1996)	SHG was elucidated for the first time in microscopic centrosymmetric particles.
Painted metal (Ying et al. 2000)	SHG spatial imaging was used to probe corrosion in painted metal to determine effectiveness of corrosion inhibitors.
Malachite green in aqueous solution (Yan et al. 2001)	Molecular transfer between microparticles was probed using SHG. The in-situ movement of malachite green in aqueous solution from spherical polystyrene microparticle surface to disk-shape clay microparticles was observed. The energy of adsorption and surface concentration was determined using adsorption isotherms through SH.

Aqueous/α-Al_2O_3 single-crystal interfaces (Fitts et al. 2005)	SHG was used to observe the pH dependency of the electrostatic charging behavior of the crystal surface.
Water/α-TiO_2(110) interface (Fitts et al. 2005)	SHG was used to characterize the pH at the surface and was found to agree with computational data.
Silica/water interfaces (Al-Abadleh et al. 2005)	SHG was used to perform hexavalent chromium real time kinetics measurements on functionalized fused silica surfaces.
Mineral oxide/water interface (Mifflin et al. 2006)	SHG was used to investigate the binding behavior of oxytetracyline to the interface.
Muscovite/water interface (Saslow Gomez et al. 2012)	SHG was used to model contaminant transport of uranyl at the interface.
Sapphire and mica/water interface (Abdelmonem et al. 2015)	SHG studies showed that at the surface of mica, a strong ice nucleator, water changes its structural arrangement past the freezing transition. On the other hand, water at the sapphire interface, a poor ice nucleator, does not exhibit such change.
Water/silica interface (Purnell and Walker 2019)	SHG results show that restricted water dynamics led to non-polar solvation behavior likened to that of solutes in confinement. When water is unable to hydrogen bond with the silica surface, solute reactivity across buried interfaces was observed to change.
Aqueous salts/silica interface (Boamah et al. 2019)	Homodyne and heterodyne SHG probing of these interfaces answered confounding questions on these types of systems such as how surface charge density is affected by ions at the interface, how phase matching is affected by ion size or ionic strength at the surface, and how ions interact with the interfacial plane based on double layer models (Ma et al. 2021; Ma and Geiger 2021).
Electrode/electrolyte interface (Xu et al. 2020)	Phase studies using SHG probes the electric field at the electrolyte-electrode interface, including potential of zero charge possessed by an electrochemical material.
Fused silica/water interface (Ma et al. 2021)	Experiments using non-resonant SHG phase and intensity measurements at varying pH indicated the presence of an additional non-linear susceptibility term called $\chi^{(3)}$, which refers to a 90° phase shift coming from charged interfaces

4. Liquid Surfaces

Since liquid surfaces and liquid-liquid interfaces are not easily studied using linear spectroscopic methods, SHG and other non-linear techniques became quite valuable in understanding these types of interfaces. Important information such as adsorption mechanisms, dielectric and transport properties and composition of the interface may be gleaned using SHG (Eisenthal 1996). Ultra-high vacuum surface techniques such as X-ray photoelectron spectroscopy (XPS), Auger electron spectroscopy (AES) and time-of-flight secondary ion mass spectroscopy (ToF-SIMS) are also not useful, as these cannot be used in volatile systems. SHG studies dealing with liquid surfaces are shown in Table 4.

Table 4: SHG Studies on liquid surfaces.

Sample	Summary
Various liquid surfaces (Wang 1969)	The very first elucidation of SHG study on liquid surfaces.
Water surface (Rasing et al. 1985)	SHG was used for the molecular orientation studies of pentadecanoic acid at the water surface.
Water surface (Rasing et al. 1985)	SHG determined that the average molecular orientation of a monolayer of sodium-dodecylnaphthalene-sulfonate on a water surface is dependent on the surface density of the molecules.
Phenol solution (Hicks et al. 1986)	Phenol molecules were found to be tilted at a 50° angle at the vapor/solution interface using SHG.
Water surface (Sitzmann and Eisenthal 1988)	Photoisomerization of (3,3'-diethyloxadicarbocyanine iodide) at the water surface were probed using SHG, where it was found to be faster at the surface than in the bulk.
Water surface (Wang et al. 1997)	SHG was used to obtain the polarity of N, N-diethyl-p-nitroaniline (DEPNA) at the surface.
Water surface (Fordyce et al. 2001)	Temperature dependence studies on polarization at the air-water interface were done using SHG.
Water surface (Rao et al. 2003)	SHG was used to determine the orientational angle and distribution in the Langmuir monolayer of a liquid crystal molecule 4-n-octyl-4-cyanobiphenyl (8CB) at the water surface.
Water surface (Dalstein et al. 2019)	Direct determination of water surface potential and surface charge density were performed using phase sensitive SHG. This method selectively probed water

	molecule reorientation in the electrical double layer in the presence of surface fields. The nonlinear relationship of the second order nonlinear susceptibility of the electrical double layer to the surface charge cannot be described, implying that the surface charge and structural properties can be investigated, separately.
Ionic liquid surface (Costa et al. 2020)	Ionic liquid surface characterization through SHG polarization-resolved analysis determined ion orientation at the surface and identified predominant ions on the surface due to alkyl chain length effect.
Water surface (Revillod et al. 2021)	Molecular aggregates in the solution of the crystal violet dye were probed using SH scattering to develop a model on nonlinear dipole assemblies. It was determined that phase retardation of the SH signal had to be accounted for to correctly describe the polarization-resolved response at the harmonic frequency.

5. Liquid-liquid Interfaces

Liquid-liquid interfaces are one of the most difficult samples to prepare, as several factors had to be considered, such as liquid density, to come up with a well-defined interface. Such systems investigated under SHG are shown in Table 5.

Table 5: SHG Studies on liquid-liquid interfaces.

Sample	Summary
Aqueous/decane and aqueous/carbon tetrachloride interfaces (Grubb et al. 1988)	The earliest recorded SHG study on liquid-liquid interfaces. SHG was used in determining the monolayer orientation of sodium 1-dodecylnaphthalene-4-sulfonate (SDNS) at the two different interfaces.
Water/1,2-dichloroethane (DCE) interface (Kott et al. 1993)	SHG was used to study the photoinduced electron transport at this interface. Trans-1-ferrocenyl-2-[4-(trimetryammonio)phenyl]-ethylene tetraphenylborate was used as the redox probe molecule. The intensity of the SHG signal depended on the degree of oxidation of the ferrocene molecule such that the addition of nitric acid at the aqueous phase led to enhanced signal intensity.
Water/dichloroethane (Higgins and Corn 1993)	SHG was used in monitoring adsorption at the interface between two immiscible electrolytic solutions (ITIES) in tandem with surface tension measurements, which allows the determination of the relative surface coverage of the surfactant 2-(n-octadecylamino)-naphthalene-6-sulfonate (ONS) at the ITIES as a function of applied potential.
n-Alkane/water interface (Conboy et al. 1994)	Total internal reflection SHG (TIR-SHG) was used for the first time to probe this interface, showing a high degree of ordering.
Water/1,2-dichloroethane interface (Conboy and Richmond 1997)	The potential induced electrolyte accumulation at the water-1,2-dichloroethane interface was probed using TIR-SHG, where the Galvani potential for ion transfer was determined using SHG data.
Heptane/water interface (Uchida et al. 2000)	SHG showed proof of molecular association of rhodamine dye at the interface, which was dependent on interfacial coverage. At the interface, the electronic dipole transition of the molecule appeared to be parallel with respect to each other.
Glycerol-water interface (Fita et al. 2009)	The effect of local viscosity at the interface on the relaxation rates of dyes malachite green and brilliant green was determined using SHG, together with transient absorption measurements. At low dye concentrations of below 10^{-5} M, the SHG signal kinetics was determined to be a mono-exponential decay, while at higher concentrations, it follows a biexponential function.
Alkane/water interface (Fedoseeva et al. 2010)	Salt effects on dye aggregates at the interface were determined using time-resolved SHG studies. The addition of sodium salts on malachite green led to aggregation enhancement at the interface.
Alkane-water interface (Martin-Gassin et al. 2011)	Monitoring of nitric acid extraction by a monoamide at the interface was done using SHG.
Aqueous NaOH/chlorobenzene interface (Fita 2014)	SHG was used to provide important insight on phase transfer catalysis (PTC) at the interface. For the first time, direct observation and identification of adsorbed species, thymolphthalein, undergoing PTC took place. Deprotonation was clearly identified to occur at the interface leading to the determination of adsorption

	and deprotonation kinetics in these types of systems.
Hexadecane-water interface (Wu et al. 2016)	SHG emission was found to mostly come from interfacial water molecules with their hydrogen atoms pointing to the oil phase.
Water/1,2-dichloroethane interface (Lin et al. 2018)	Supramolecular formation at the interface was probed using SHG. Results show that 5-octadecyloxy-2-(2-pyridylazo)phenol (PARC18), though achiral as a monomer, forms a chiral supramolecular structure at the interface. Enantiomeric excess was determined by the twist angle of PARC18 molecules at the interface rather than their surface orientational angle.
Oil/water interface (Wu et al. 2019)	Particulate matter studies involving polystyrene nanoparticles between the interface was done using time-resolved SHG. Depending on the charge of the particles predominant at the interface, SHG emission signal varied.

6. Buried Interfaces

SHG has been proven to be useful in investigating buried solid-solid interfaces, which are typically inaccessible by other optical techniques. Table 5 shows SHG studies that probed this type of system.

Table 6: SHG Studies on buried interfaces.

Sample	Summary
CaF_2/Si(111) interface (Himpsel et al. 1989)	One of the earliest examples of studies concerning these interfaces. It was proven that a 2-D band structure of an interface can be determined. SHG was used to detect inter-band transition across the band gap between bonding and anti-bonding interface states, which was determined to have an interfacial bandgap value of 2.4 eV.
Si/SiO_2 interface (Aktsipetrov et al. 1994)	The first elucidation of electric field-induced SHG at the Si-SiO_2 interface. Direct current electric field was applied to the interface with metal-oxide-semiconductor (MOS) structures to determine the effects of electroinduction on the SHG signal.
Au/GaAs interface (Rasing 1994)	SHG signal intensity was found to be dependent on the applied bias. Schottky barrier height, and the sweepout carriers coming from the femtosecond excitation affected the signal. On the other hand, metallic interfaces such as Cu-Co-Cu multilayers were found to be strongly dependent on interfacial magnetization.
Si/SiO_2 interface (Vanbel et al. 2014)	SHG was used to monitor the manipulation and enhancement of MOS properties for device production.
Graphite film interfaces (Lam et al. 2018)	Soft X-ray SHG has been used to probe graphite film interfaces. The technique shows interfacial and elemental specificity, providing a new tool for probing various buried interfaces.
GaP(001)/Si(001) interfaces (Brixius et al. 2018)	SHG was used to show the direct relationship between SHG response and interface heterostructure quality. Results show that SHG with TEM may be used as in-situ techniques to monitor epitaxial growth to detect twinning and anti-phase domains.
Boron nitride crystals (Yao et al. 2021)	SHG served as a reliable probe for twistable van der Waals interfaces or twistoptics. Rotatable stacks of the crystals at various stacking angles allows control of the presence or absence of inversion symmetry leading to tunable frequency generation.

7. Imaging and Chiral SHG

Examples of SHG for chirality and imaging studies are shown in Table 7.

Table 7: SHG imaging and chirality studies.

Sample	Summary
Chiral molecules at air/water interface (Petralli-Mallow et al. 1993)	One of the earlier attempts to use SHG circular dichroism (SHG-CD), wherein a series of chiral molecules at the air-water interface were studied. A comparison between SHG with the standard method CD spectroscopy showed that the former generated signal magnitudes 10^3 times greater than the latter.
R- and S-2,2'-dihydroxyl-1,1'binaphthyl (BN) chiral monolayers (Byers et al. 1994)	SHG efficiency of oriented chiral molecules was found to be dependent on the handedness of the incoming excitation beam.
Melittin adsorbed to 1-palmitoyl-2-oleoyl-sn-glycero-3-phosphotidylcholine (POPC) (Zhu et al. 1988)	Chiral SHG was applied to chiral imaging studies. The major advantage of SHG in chiral detection is that it does not require chromophore labels, or any labelling methods commonly used in

	linear spectroscopic methods. The binding properties of melittin and its affinity to POPC were studied. The second order non-linear contributions from chiral and achiral molecules were successfully separated.
Cytochrome c adsorbed at membrane surfaces (Petralli-Mallow et al. 2000)	SHG-CD was used to look at the adsorption and redox properties of the sample.
Interfaces and thin films (Simpson 2004)	Three general models concerning the chiroptical phenomena in SHG were discussed; magnetic-dipole effects arising from helical electron motion, electric-dipole effects arising from chirality within the chromophore, and electric-dipole effects arising from supramolecular orientation.
Langmuir−Blodgett thin films (Huttunen et al. 2010)	Surface chirality was characterized using focused circularly-polarized light, called SHG circular-difference phenomenon. It was observed that the technique proved to be sensitive only to chirality, and not to anisotropy.
Aerosols from the Amazon Basin (Martinez et al. 2011)	Chirality studies using SHG were applied to atmospheric chemistry through imaging work. The presence of chiral groups was confirmed in secondary aerosols sampled from the Amazon Basin, which may have implications to climate-related properties.
Optical metamaterials (Valev et al. 2011)	SHG was used to look at handedness of optical metamaterials. Numerical simulation work was used to determine the origin of the SH signal. Results show that electromagnetic field local enhancement at the fundamental frequency led to signal generation, which is very much dependent on structural pattern present on the metamaterial.
Iodobutane (Baykusheva et al. 2019)	Chiral SHG was used to monitor real time handedness evolution in the photodissociation of iodobutane. Changes in the chirality of the molecules were observed as they were undergoing chemical reaction at the femtosecond scale.
Chiral supramolecular assemblies (Xue et al. 2020)	SHG was used to monitor the formation of chiral supramolecular assemblies, such as that of copper metals and amphiphilic Schiff bases.

8. Membranes

SHG is a valuable tool in studying phospholipid membrane and liposome dynamics. Information derived using SHG on interfacial interactions, transport, and translocation in membranes are valuable in drug design and delivery, as well as in understanding various cellular membrane processes. Table 8 shows SHG studies involving membranes.

Table 8: SHG studies on membranes.

Sample	Summary
Langmuir-Blodgett monolayers of styryl dyes (Huang et al. 1988) and lipid bilayers stained with chiral styryl dyes (Bouevitch et al. 1993)	Demonstrated voltage detection across lipid membranes using SHG. The electronic response of the induced dipole of the dye to applied external electric field were observed to correlate very well, leading to the conclusion that SHG may be used to detect membrane potential using these dyes.
Malachite green (Srivastava and Eisenthal 1998)	SHG spectroscopy was performed to observe real time transport of malachite green across a bilayer of dioleoylphosphatidylglycerol liposome in aqueous solution. SHG was used to monitor the movement of the dye from the outer surface to the inner liposome surface using the decay of SH signal over time.
Oxaxole dye (Salafsky and Eisenthal 2000)	The first demonstration on the use of SHG to probe supported lipid bilayers. The adsorption of the dye to phospholipid bilayers on glass was determined. Using null angle technique, the orientation of the dye was found to be around 19° from the surface normal, when it adsorbed to the membrane.
Malachite green (Yan and Eisenthal 2000)	The effect of cholesterol on the transport kinetics of malachite green across a liposome membrane was determined.
Dioleoylphosphatidylglycerol (Liu et al. 2008)	The first demonstration of the use of the Eisenthal technique. The Eisenthal technique, which probes $\chi^{(3)}$ SHG contribution of the surface potential coming from surface to bulk solvent molecular arrangement, is particularly important in understanding membrane dynamics (Ong et al. 1992; Yan et al. 1998; Chen et al. 2012). The equation that expresses SHG electric field with this type of contribution is shown in Equation 23. In

	this equation $\Phi(0)$ is the surface potential. $E_{SHG} \sim P_{SHG} = \chi^{(2)} E_\omega E_\omega + \chi^{(2)} E_\omega E_\omega \Phi(0)$ (23) The outer surface potential and the surface density of the sample were determined. The resulting charge density of ~1.3 x 10^{14} per cm^2 or area of 70 $Å^2$/charge, actually corresponded to a lipid headgroup.
Neuron membrane (Nguyen et al. 2009)	The first demonstration on the use of SHG to image neuron membrane potential called SH retinal imaging of membrane potential (SHRIMP).
Tetracaine supported bilayer (Nguyen and Conboy 2011)	Using counterpropagating SHG imaging and with a 3D continuous flow microspotter to prepare the bilayers, the lipid phase and the cholesterol content effects on tetracaine binding were simultaneously determined. Results were able to show how SHG can directly image and quantitatively measure binding affinity to a multicomponent lipid bilayer array, demonstrating the use of SHG as a high throughput technique in measuring drug-lipid bilayer interactions.
Selective estrogen receptor modulator interactions (SERMs) (Stokes and Conboy 2014)	The equilibrium association or binding constants of SERMs such as raloxifene were determined in this study. Different lipid compositions were used to determine the effect of lipid phase, packing density, and cholesterol content.
Oils on lipid membrane (Tarun et al. 2018)	SH and white light imaging was used to observe how oils such as hexadecane and squalene redistribute in the lipid membrane. Different oil molecular structure gave different coupling mechanisms within the membrane.
Lipid membrane (Tarun et al. 2018)	Non-resonant SH response of water molecules aligned through charge-dipole interactions with the charge moiety of lipids served as label-free probes of membrane structure and dynamics. Hydration of the membranes at millisecond time scale was observed, including spatiotemporal fluctuations of membrane surface potential in the order of 100 mV.
Proteins bound to lipid bilayers (McGeachy et al. 2018)	The Eisenthal technique was used to count charges of proteins bound to lipid bilayers. SHG and atomistic simulation results were able to elucidate protein orientation on the surface, indicating that the cationic proteins neutralized the surface charge density of the bilayer. The study also proved that in this case, the Guoy-Chapman model is semi-quantitatively valid.
Malachite green isothyiocyanate (Hamal et al. 2019)	SHG spectroscopy was utilized to investigate the adsorption and transport of the sample through liposome bilayers of different compositions. In combination with molecular dynamics simulations, adsorption isotherms and transport kinetics were determined to be dependent on electrostatic interactions, ion-pair formation, and hydrophobic and hydrophilic forces.
Poly(allylamine hydrochloride) (PAH) on supported lipid bilayers (Chang et al. 2020)	SHG was used to demonstrate direct measurement of charge reversal in lipid bilayers. Heterodyne-SHG served as an interfacial optical voltmeter, where the exact charge and magnitude of the surface potential, and the point of charge reversal was determined in cationic PAH on the bilayer.
Cell membrane (de Coene et al. 2022)	The Eisenthal method was used to probe surface potential in live cells. Results show a clear correlation between SHG signal and cell membrane voltage applied through voltage clamping. This study shows that membrane hydration plays a minor contribution to field sensitivity, pointing towards lipid bilayer asymmetry as the more predominant contributor.

9. Nanomaterials

In 2000, SHG studies on nanomaterials started emerging. Work on various types of nanoscale samples were performed, such as dielectric nanoparticles, plasmonic nanostructures, substrate supported, as well as hybrid dielectric-plasmonic nanomaterials (Bonacina et al. 2020). Examples of these studies are shown in Table 9.

Table 9: SHG studies on nanomaterials.

Sample	Summary
Nano-scale polycrystalline ferroelectric films (Smolyaninov et al. 2001)	The first demonstration of SHG from nanomaterials using SH near field microscopy.
Nanoscale metal tip (Bouhelier et al. 2003)	The very first demonstration on how enhanced fields resulted to SHG. Strong light confinement at the very end of the metal tip led to a locally enhanced SH source that can be readily explained using an on-axis oscillating dipole model.
Au nanoparticles (Nappa et al. 2005)	Polarization-resolved hyper-Raleigh SHG scattering of the sample exhibited signal retardation effects in larger particles, and shape deformation effects on the generated signal.
$BaTiO_3$ nanocrystals (Pantazis et al. 2010)	The sample was used as nanoprobes for SHG imaging in zebra fish embryos. The combination of SH and nanoparticles in bioimaging showed the absence of photobleaching in addition to a highly coherent response. The generated emission is flexible at extended wavelength excitation, spectrally narrow at multiple harmonic order, and sensitive to polarization. These allow for long-term imaging of biological tissues at minimal water absorption, without autofluorescence. In vivo imaging in the presence of the nanoprobes showed long term photostability, the absence of blinking and bleaching of the images, as well as a stable signal that does not saturate at high intensity incoming beam.
Ultrathin metasurfaces and 2D materials (Krasnok et al. 2018; Bonaccorso et al. 2010; Manzeli et al. 2017)	SHG was also used to analyze metasurfaces and 2D materials, as well as layering of these materials. Lithographic techniques allow for the design of metasurfaces that have varying SHG responses. 2D materials made of graphene and chalcogenides exhibited unique optical properties and intense SHG response.
Plasmonic nanocups made of silica nanoparticles capped with gold (Zhang et al. 2011)	SHG coming from these nanostructures changed direction with nanoparticle orientation, and increased in intensity with angular difference between incoming beam and nanoparticle symmetry axis.
CdSe quantum dots (Peterson et al. 2011)	Not all of the quantum dots generated signal, which could be attributed to distribution or aggregation of the sample.
Trans-4-[4-(dimethylanime)-N-mthylstilbazolium]p-tosylate organic nanocrystals (Zheng et al. 2011)	SHG was used in tandem with two-photon fluorescence to analyze the samples, which are currently studied for their high electro-optical properties.
Au nanoantennas (Butet et al. 2013)	SHG revealed asymmetry and surface roughness by far-field analysis.
$BaTiO_3$ nanoprobes (Liu et al. 2014)	The quantification of mRNA in human cells was performed with $BaTiO_3$ nanoprobes using a technique called SH super-resolution microscopy (SHaSM). The technique was able to detect a single mRNA and resolve multiple copies at a diffraction-limited spot, overcoming resolution limitations in microscopy.
Doubly resonant single crystalline gold nanostructures (Celebrano et al. 2015)	The lack of phase matching in nanoplasmonics was addressed using the sample, which are axial-symmetry deficient. With mode matching, observed SHG enhancement in these systems was seen at 3×10^6 photons per second.
Nano-objects (Duboisset and Brevet 2019)	SHG scattering was used to determine nanoparticle topology. Balance between nanoparticles symmetry and size were found to define measured scattered SHG.
ZnO nanowires (Wang et al. 2019)	Polarized SHG (p-SHG) was used to observe the directional assembly of the sample, demonstrating the nondestructive, rapid, in situ, and polarization-resolved characterization of functional devices.
Crystals with self-assembled Au nanoparticles (Gürdal et al. 2020)	SHG behavior of the samples were investigated, where at the plasmon resonance, the observed SHG signal went up to as high as 60-fold.
Harmonophores which are made up of protein nanotubes encapsulated in sodium dodecyl sulfate (SDS) and poly(L-lactic acid) (PLLA) (Sonay et al. 2021)	A very high resolution SHG technique was developed using biodegradable nanoprobes called harmonophores. These markers targeted single cancer cells with high detection sensitivity in vivo for zebra fish embryos. This showed an innovative approach to cancer imaging.
Te nanosheets (Wang et al. 2021)	The sample shows significant nonlinear optical response showing potential to be used as effective

	nonlinear photonic and optoelectronic nanodevices.
Au and ZnO metamaterials (Li et al. 2021)	SHG studies on these samples provide enhanced signal at the visible range. The array of metal and dielectric alternating pattern led to giant field localization due to broadband and efficient coupling of light called "rainbow trapping" or frequency-dependent spatially localized slow light.
Ultrathin GaP metasurface (Shcherbakov et al. 2021)	A record high enhanced high harmonic generation was achieved using nanostructure hotspots. Even and odd harmonics were generated covering a wide range of photon energies from 1.3-3 eV at minimal reabsorption.
Ag nanoparticle arrays ion-implanted on glass (Chu et al. 2022)	SHG studies on cost-efficient, readily fabricated, and environmentally-stable nano-optical devices such as the ones in this study, are important trends in optical materials development and design.
0D chiral hybrid indium halide materials (Qi et al. 2022)	These samples were designed as non-linear optical materials, which were characterized using SHG. Results show that these new materials have strong harmonic responses, and low damage threshold.
Au nanoparticles (Ali et al. 2023)	A 32-fold SHG signal increase was observed when the sample was coated on mesoporous $LiNbO_3$ microspheres. This occurred without the use of nanoantennas, which require precision nanofabrication, opening new doors for subwavelength nonlinear optical platforms.
Graphene (Lu et al. 2023)	The lattice of graphene was manipulated to induce sublattice polarization to generate SH. The straining of graphene on nanopillar structures resulted in the 30% increase of the second order non-linear susceptibility tensor with respect to that of the hexagonal boron nitride monolayer.

10. Biological Samples

SHG imaging is advantageous for examining biological samples, as it is a label-free technique that provides enhanced image contrast (Murakami et al. 2022). Table 10 shows examples of studies utilizing SHG for microscopy studies.

Table 10: SHG studies on biological samples.

Sample	Summary
Rattail tendon (Freund and Deutsch 1986)	The first recorded study using SHG imaging on biological samples. Images were able to clearly elucidate that the tendon comprises mostly of fine polar filamentous structures and some very polar surface patches.
Liver tissue (Cox et al. 2003)	SHG imaging was used to study collagen in the liver. The results show that SHG is able to discriminate between collagen type 1 and type 2.
Various histological samples (Campagnola 2011)	SHG was used in detecting fibrosis of internal organs. SHG imaging was found to be more advantageous compared to standard histological scoring procedures for imaging fibrosis since it can obtain 3D image sets of the tissues that are provide additional medical information.
Tumor tissue (Lukina et al. 2019)	SHG imaging was used to monitor tumor response to chemotherapy.
Proteins (Kaneshiro et al. 2019)	SHG microscopy was used to analyze protein structure.
Scar tissues (Pham et al. 2020)	SHG was used to determine the effectiveness of electrochemical therapy (ECT), which is a method to treat scars. ECT is a simple, low-cost, and minimally invasive process that alters collagen structure to remodel skin. Loss of SHG signal on the anode side and emission of SHG signal on the cathode side showed the ability of ECT to alter collagen structure through denaturation (Nemet et al. 2004).
Liver tissue (Zhuang et al. 2020)	Using SHG in tandem with TPEF to differentiate hepatic steatosis distribution patterns between healthy and fatty liver.
Chromatin (Yamin et al. 2020)	SHG microscopy was used to observe chromatin organization in live yeast cells.
Starch granules (Chakraborty et al. 2020)	SHG was used to investigate the molecular structure and mechanical properties of starch granules.
Membranes (Zhang et al. 2020)	SHG was used for the imaging of membrane potential due to membrane response to applied potential. An imaging technique called SH Retinal Imaging of Membrane Potential (SHRIMP) was

	developed, which is capable of producing high-resolution images of live neuronal membranes and a voltage map of local trans-membrane potential.
Lung tumor cells (van Huizen et al. 2020)	Fresh lung tumors were probed using SHG, generating 3D real-time high-resolution images. This demonstrated the possibility of reducing operation time and endoscopy in lung cancer treatment.
Collagen (Johnson et al. 2021)	Super resolution SHG (SR-SHG) detection of nanoscale changes in collagen was performed using photonic nanojet, which may have significant implications in processes such as drug delivery.
Mouse lung tissue (Mostaco-Guidolin et al. 2021)	SHG was used to differentiate between healthy and emphysematous tissue. Results show that through collagen fiber organization within sub-pleural alveolar ducts, lung health assessment can be performed.
Fixed tissues (Hristu et al. 2022)	Polarization-resolved SHG (PSHG) microscopy with image processing techniques and computationally generated 2D SHG images using single-axis molecule model for collagen called PSHG-TISS, provided additional quantitative explanations on collagen structure and distribution. Generated images complemented qualitative explanations derived from SHG collagen images.
Tumor tissue (Mirsanaye et al. 2022)	Use of PSHG and texture analyses using machine learning resulted in a 94.2% accuracy in differentiating normal tissue from tumor tissue.
Drosophila melanogaster larvae body wall muscles (Karunendiran et al. 2022)	The effect of myosin content in the ultrastructure of the sample was studied using linear polarization-in polarization-out (PIPO) SHG.

HOME-BUILT SHG MICROSCOPE

The schematic diagram of the recently built SHG microscope is shown in Figure 5. The design follows a counterpropagating beam geometry, which allows tuning of the incoming beam's polarization. These are particularly important for surface chirality studies, and polarization mapping studies. This type of beam geometry is also known to have better image magnification and resolution, compared to other beam geometry design (Flörsheimer 1999). The set-up is optimized for the imaging of collagen in marine samples, ensuring that sample degradation or burning does not happen during the image acquisition process. SHG allows for direct imaging of samples, without prior sample preparation such as staining, making it quite advantageous for *in situ* analyses (Manzeli et al. 2017; Qi et al. 2022; Lu et al. 2023).

The laser source used in the set-up is an Ekspla Nd-YAG laser with a 1064 nm fundamental beam, pulse duration of 28 ± 10% ps, and pulse repetition rate of 50 Hz. High energy Nd-YAG mirrors were used to guide the beams towards the sample. To achieve a counter propagating geometry, a beam splitter was used to separate the beams into opposite directions, using lenses to ensure that the energies of the incoming beams are similar. A time delay stage is used to ensure spatial and temporal overlap of the two beams on the sample. Incoming angles are set at $\theta = \theta' \sim 23^{o}$, following theoretical calculation results shown in Figure 4. The detector used was an Andor iKon-M 934 mounted on a Nikon Eclipse E200 modified upright microscope.

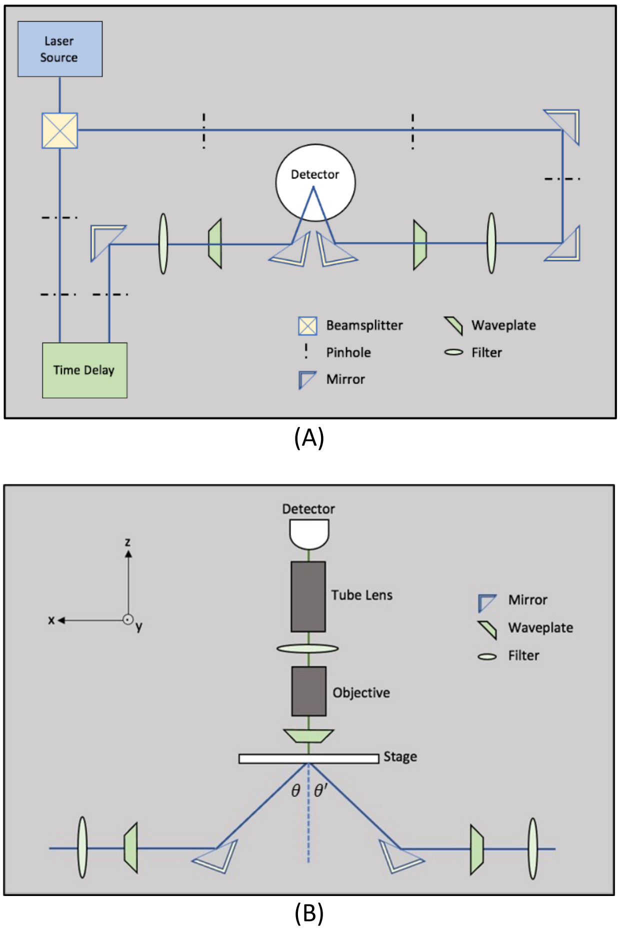

Figure 5: Schematic diagram of the SHG set-up path (A) and the detector system (B).

The ability of the microscope to generate SHG signal was demonstrated using a BBO crystal, a known SHG generator. The SHG image of BBO is shown in Figure 6. Calibration of the set-up was done using z-cut quartz, another known SHG generator, shown in Figure 7. To confirm the counterpropagating geometry of the set-up, the two beam paths were alternately block to see if the SH signal disappears. Furthermore, a USAF resolution test chart was imaged to determine the resolution of the set-up shown in Figure 8. The lowest resolution available in the test chart (1.1 µm/line pair) was observed using the microscope.

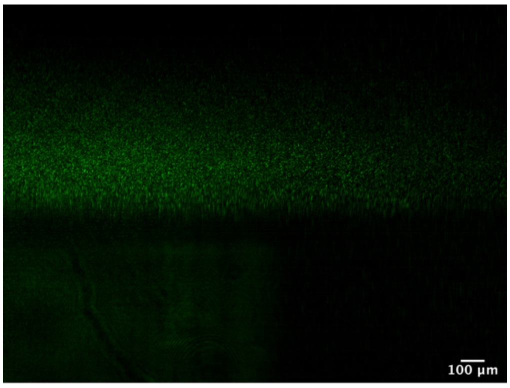

Figure 6: SHG image of a BBO crystal.

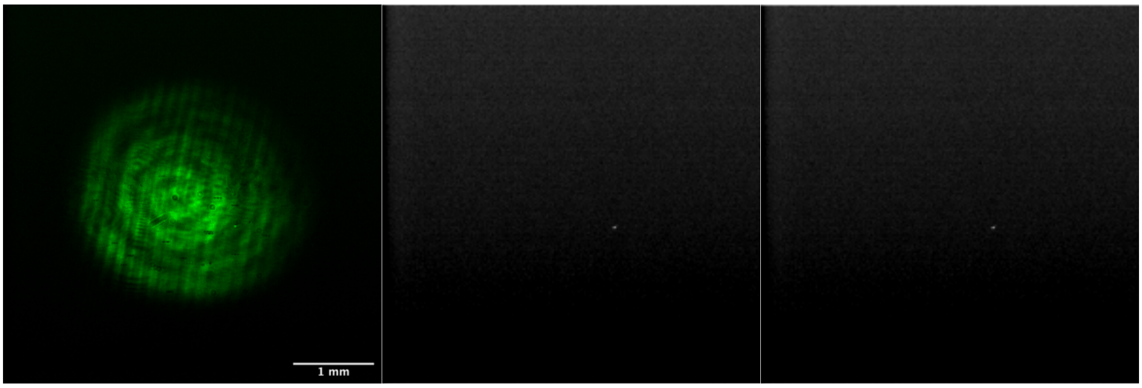

(A) (B) (C)

Figure 7: SHG image of (A) z-cut quartz (in false color). Absence of signal when one beam path (B) or the other (C) is blocked.

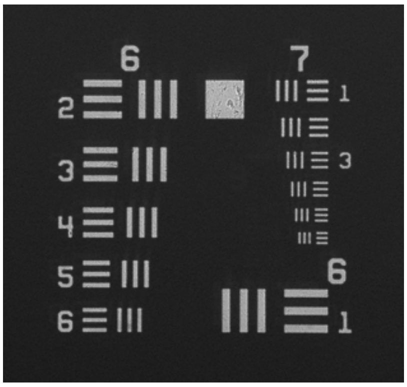

Figure 8: SHG image of (A) z-cut quartz (in false color). Absence of signal when one beam path (B) or the other (C) is blocked.

Biological samples tested for imaging are collagen from fish scales of milkfish (*Chanos chanos*), mutable collagenous tissue of sea cucumbers (*Stichopus horrens cf*), and extracted collagen from sea cucumbers (*Stichopus horrens cf*). Figure 9 shows SHG images taken from the home-built microscope. The distribution of collagen in each of the samples reflects the signal generating sites in the images. For example, the SHG image of the fish scale in Figure 9a shows SHG-active collagen situated on its grooves. The set-up has the potential to study different biomaterials, including environmental effects on various species with collagen and SHG active components. The microscope also has the potential to investigate other systems such as interfaces, nanomaterials, and charged samples.

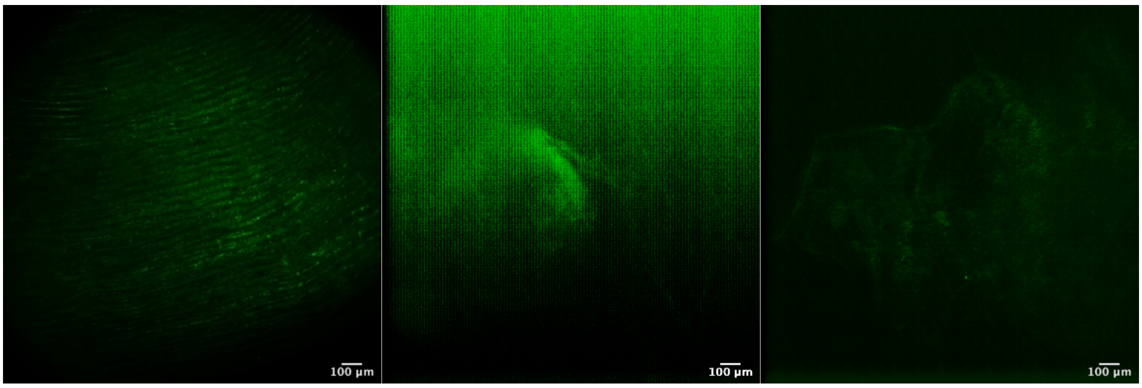

(A) (B) (C)

Figure 9: SHG image of (A) fish scale, (B) extracted collagen, and (C) mutable collagenous tissue of sea cucumbers (in false color).

SUMMARY AND CONCLUSION

Interfacial studies using SHG are of high importance because of the information these types of work can provide on surface mechanisms and surface molecular orientation. In this paper, basic theoretical framework on SH signal generation was presented. Calculation results performed in this study was also shown in terms of SHG intensity at different outgoing beam polarization angles for different molecular symmetries. Three factors that affect SHG signal generation are given emphasis in this paper, which are molecular symmetry, optical set-up or beam geometry, and beam polarization. These are particularly vital for the basic understanding of beginners in this field.

On the sample studies presented, it can be observed that most of the earlier works were concerned with mechanisms and interactions occurring at the interface. Bulk of these studies involved biochemical systems and metal surfaces. The target applications mostly involved adsorption on interfaces and material transport between two phases. Afterwards, the use of this technique went to semi-metal systems, expanding its usage to many industrial applications, which rely on samples such as semiconductors. Another important turning point in SHG was its use in the detection of chirality in molecules, followed by applications in imaging. This broadened further the range of applications using this technique, such as the analysis of chiral organic molecules, medical studies on biological systems and nanomaterials. Currently, there are hundreds of papers related to SHG spectroscopy and imaging. The latest of these research works were on biological samples and drug delivery systems. Studies using scattering SHG on nanomaterials, molecular thin films, aerosols, liposomes, and biological cells are also being done (Wilhelm and Dai 2021). Moreover, material design for SH signal enhancement, frequency tuning of emission, as well as the understanding of signal contributions will always be important in SHG studies.

Lastly, a counterpropagating geometry SHG microscope was recently built, which can open new avenues of research in the country. It is currently optimized to probe collagen in biomaterials. However, it can also be used to look at other interesting samples, such as interfaces, nanomaterials, and novel SH generating materials.

ACKNOWLEDGMENTS

The authors would like to acknowledge funding provided by the Natural Sciences Research Institute (CHE-19-1-03), the Department of Science and Technology (DOST)–PCAARRD, DOST-PCIEERD, and the DOST–Industrial Technology Development Institute for personnel support.

CONTRIBUTIONS OF INDIVIDUAL AUTHORS

Imee Su Martinez: Conceptualization, Resources, Writing – Original Draft, Writing – Review & Editing, Supervision, Funding Acquisition. **Allen Marbert S. Lee:** Investigation, Writing – Original Draft.

CONFLICTS OF INTEREST

The authors listed certify that there are no known conflicts of interest in this study.

REFERENCES

Abdelmonem A, Lützenkirchen J, Leisner T. Probing ice-nucleation processes on the molecular level using second harmonic generation spectroscopy. Atmos Meas Tech 2015; 8(8): 3519-3526.

Aktsipetrov OA, Fedyanin AA, Golovkina VN, Murzina TV. Optical second-harmonic generation induced by a DC electric field at the Si–SiO2 interface. Opt Lett 1994; 19(18):1450-1452.

Al-Abadleh HA, Mifflin AL, Musorrafiti MJ, Geiger FM. Kinetic studies of chromium (VI) binding to carboxylic acid- and methyl ester-functionalized silica/water interfaces important in geochemistry. J Phys Chem B 2005. 109(35):16852-16859.

Ali RF, Busche JA, Kamal S, Masiello DJ, Gates BD. Near-field enhancement of optical second harmonic generation in hybrid gold–lithium niobate nanostructures. Light Sci Appl 2023; 12(1):99.

Anderson RJM, Hamilton JC. Azimuthally resolved optical second-harmonic generation from hydrogen on nickel (111). Phys Rev B 1988; 38(12):8451-8454..

Baykusheva D, Zindel D, Svoboda V, Bommeli E, Ochsner M, Tehlar A, Wörner HJ. Real-time probing of chirality during a chemical reaction. Proc Natl Acad Sci USA 2019; 116(48): 23923-23929.

Benninghoven A. Analysis of submonolayers on silver by negative secondary ion emission. Phys Stat Sol B 1969; 34(2):K169-171.

Berg JC. An Introduction to Interfaces and Colloids: The Bridge to Nanoscience. New Jersey: World Scientific, 2009:773.

Biwer BM, Pellin MJ, Schauer MW, Gruen DM. Electrochemical and second harmonic generation investigation of nickel corrosion in 0.1 M NaOH. Surf Interface Anal 1989; 14(10): 635-646.

Biwer BM, Pellin MJ, Schauer MW, Gruen DM. A second harmonic generation study of the iron electrode surface using a picosecond laser. Surface Sci 1986; 176(1–2): 377-396

Bloembergen N, Pershan PS. Light waves at the boundary of nonlinear media. Phys Rev 1962; 128(2): 606-622.

Boamah MD, Ohno PE, Lozier E, Van Ardenne J, Geiger FM. Specifics about specific ion adsorption from heterodyne-detected second harmonic generation. J Phys Chem B 2019; 123(27): 5848-5856.

Bonaccorso F, Sun Z, Hasan T, Ferrari AC. Graphene photonics and optoelectronics. Nat Photonics 2010; 4(9): 611-622.

Bonacina L, Brevet P, Finazzi M, Celebrano M. Harmonic generation at the nanoscale. J Appl Phys 2020; 127(23): 230901.

Bouevitch O, Lewis A, Pinevsky I, Wuskell JP, Loew LM. Probing membrane potential with nonlinear optics. Biophys J 1993; 65(2): 672-679.

Bouhelier A, Beversluis M, Hartschuh A, Novotny L. Near-field second-harmonic generation induced by local field enhancement. Phys Rev Lett 2003; 90(1): 013903.

Boyd R. Nonlinear Optics. 4th ed. Cambridge:Academic Press. 2020.

Boyd R. Nonlinear Optics. 3rd ed. Cambridge:Academic Press. 2008.

Bradley RA, Friedrich KA, Wong EKL, Richmond GL. A comparative second harmonic study of Cu(111) in UHV and in solution. J Electroanal Chem Interfacial Electrochem 1991; 309(1–2): 319-324.

Brixius K, Beyer A, Mette G, Güdde J, Dürr M, Stolz W, Volz K, Höfer U. Second-harmonic generation as a probe for structural and electronic properties of buried GaP/Si(0 0 1) interfaces. J Phys Condens Matter 2018; 30(48): 484001.

Brown F, Matsuoka M. Effect of adsorbed surface layers on second-harmonic light from silver. Phys Rev 1969; 185(3): 985-987.

Brown F, Parks RE, Sleeper AM. Nonlinear optical reflection from a metallic boundary. Phys Rev Lett 1965; 14(25): 1029-1031.

Buck M, Grunze M, Eisert F, Fischer J, Träger F. Adsorption kinetics of n -alkyl thiols on gold studied by second harmonic generation and x-ray photoelectron spectroscopy. J Vac Sci Technol A 1992; 10(4): 926-929.

Butet J, Thyagarajan K, Martin OJF. Ultrasensitive optical shape characterization of gold nanoantennas using second harmonic generation. Nano Lett 2013; 13(4): 1787-1792.

Byers JD, Yee HI, Hicks JM. A second harmonic generation analog of optical rotatory dispersion for the study of chiral monolayers. J Chem Phys 1994; 101(7): 6233-6241.

Byers JD, Yee HI, Petralli-Mallow T, Hicks JM. Second-harmonic generation circular-dichroism spectroscopy from chiral monolayers. Phys Rev B 1994; 49(20):14643-14647.

Campagnola PJ. Second harmonic generation imaging microscopy: applications to diseases diagnostics. Anal Chem 2011; 83(9): 3224-3231.

Campagnola PJ, Loew LM. Second-harmonic imaging microscopy for visualizing biomolecular arrays in cells, tissues and organisms. Nat Biotechnol 2003; 21(11): 1356-1360.

Campbell DJ, Corn RM. Second harmonic generation studies of hydrogen evolution from polycrystalline silver electrodes in acetonitrile. J Phys Chem 1987; 91(22): 5668-5673.

Campbell DJ, Higgins DA, Corn RM. Molecular second harmonic generation studies of methylene blue chemisorbed onto a sulfur-modified polycrystalline platinum electrode. J Phys Chem 1990; 94(9): 3681-3689.

Celebrano M, Wu X, Baselli M, Großmann S, Biagioni P, Locatelli A, De Angelis C, Cerullo G, Osellame R, Hecht B, Duò L, Ciccacci F, Finazzi M. Mode matching in multiresonant plasmonic nanoantennas for enhanced second harmonic generation. Nat Nanotechnol 2015; 10(5): 412-417.

Chakraborty I, Pallen S, Shetty Y, Roy N, Mazumder N. Advanced microscopy techniques for revealing molecular structure of starch granules. Biophys Rev 2020; 12(1): 105-122.

Chang H, Ohno PE, Liu Y, Lozier EH, Dalchand N, Geiger FM. Direct measurement of charge reversal on lipid bilayers using heterodyne-detected second harmonic generation spectroscopy. J Phys Chem B 2020; 124(4): 641-649.

Chen CK, Heinz TF, Ricard D, Shen YR. Detection of molecular monolayers by optical second-harmonic generation. Phys Rev Lett 1981; 46(15): 1010-1012.

Chen C, Lin Z, Wang Z. The development of new borate-based UV nonlinear optical crystals. Appl Phys B 2005; 80(1): 1-25.

Chen EH., Saslow SA, Nguyen ST, Geiger FM. Zinc ion–hydroxyl interactions at undecanol-functionalized fused silica/water interfaces using the Eisenthal χ(3) technique. J Phys Chem C 2012; 116(12): 7016-7020.

Chen J, Hu C, Kong F, Mao J. High-performance second-harmonic-generation (SHG) materials: new developments and new strategies. Acc Chem Res 2021; 54(12): 2775-2783.

Cheng X, Li Z, Wu X, Hong M, Whangbo M, Deng S. Key factors controlling the large second harmonic generation in nonlinear optical materials. ACS Appl Mater Interfaces 2020; 12(8): 9434-9439.

Chu L, Li Z, Zhu H, Ren F, Chen F. Second-harmonic generation of embedded plasmonic nanoparticle arrays via interparticle coupling. Appl Phys Lett 2022; 120(7): 073104.

de Coene Y, Jooken S, Deschaume O, Van Steenbergen V, Berghe PV, den Haute CV, Baekelandt V, Callewaert G, Van Cleuvenbergen S, Verbiest T, Bartic C, Clays K. Label-free imaging of membrane potentials by intramembrane field modulation, assessed by second harmonic generation microscopy. Small 2022; 18(18): 2200205.

Cole WTS., Wei H, Nguyen SC, Harris CB, Miller DJ, Saykally RJ. Dynamics of micropollutant adsorption to polystyrene surfaces probed by angle-resolved second harmonic scattering. J Phys Chem C 2019; 123(23): 14362-14369.

Collins RJ, Nelson DF, Schawlow AL, Bond W, Garrett CGB, Kaiser W. Coherence, narrowing, directionality, and relaxation oscillations in the light emission from ruby. Phys Rev Lett 1960; 5(7): 303-305.

Conboy J, Daschbach J, Richmond G. Studies of alkane/water interfaces by total internal reflection second harmonic generation. J Phys Chem 1994; 98(39): 9688-9692.

Conboy JC, Richmond GL. Examination of the electrochemical interface between two immiscible electrolyte solutions by second harmonic generation. J Phys Chem B 1997; 101(6): 983-990.

Corn RM, Higgins DA. Optical second harmonic generation as a probe of surface chemistry. Chem Rev 1994; 94(1): 107-125.

Costa R, Pereira CM, Silva AF, Brevet P, Benichou E. Ordering and nonideality of air–ionic liquid interfaces in surface second harmonic generation. J Phys Chem B 2020; 124(19): 3954-3961.

Cox G, Kable E, Jones A, Fraser I, Manconi F, Gorrell MD. 3-dimensional imaging of collagen using second harmonic generation. J Struct Biol 2003; 141(1): 53-62.

Dalstein L, Chiang K, Wen Y. Direct quantification of water surface charge by phase-sensitive second harmonic spectroscopy. J Phys Chem Lett 2019; 10(17): 5200-5205.

Driscoll TA, Perkins PE, Hoffman HJ, Stone RE. Efficient second-harmonic generation in KTP crystals. J Opt Soc Am B 1986; 3(5): 683-686.

Duboisset J, Brevet P. Second-harmonic scattering-defined topological classes for nano-objects. J Phys Chem C 2019; 123 (41): 25303-25308.

Eckardt RC. Nonlinear optics, basics | χ(2)–harmonic generation. In: Guenther RD, Steel DG, eds. Encyclopedia of Modern Optics. 1st ed. Amsterdam:Elsevier, 2005: 213-23.

Eckenrode HM, Jen S, Han J, Yeh A, Dai H. Adsorption of a cationic dye molecule on polystyrene microspheres in colloids: effect of surface charge and composition probed by second harmonic generation. J Phys Chem B 2005; 109(10): 4646-4653.

Eisenthal KB. Liquid interfaces probed by second-harmonic and sum-frequency spectroscopy. Chem Rev 1996; 96(4): 1343-1360.

Fang Y, Fu R, Tang H, Shui Q, Ma Z, Wu X. Titanium iodates with a second-harmonic-generation response. Inorg Chem 2021; 60(8): 5821-5828.

Fedoseeva M, Fita P, Punzi A, Vauthey E. Salt effect on the formation of dye aggregates at liquid/liquid interfaces studied by time-resolved surface second harmonic generation. J Phys Chem C 2010; 114(32): 13774-13781.

Fita P. Toward understanding the mechanism of phase transfer catalysis with surface second harmonic generation. J Phys Chem C 2014; 118(40): 23147-23153.

Fita P, Punzi A, Vauthey E. Local viscosity of binary water+glycerol mixtures at liquid/liquid interfaces probed by time-resolved surface second harmonic generation. J Phys Chem C 2009; 113(48): 20705-20712.

Fitts JP, Machesky ML, Wesolowski DJ, Shang X, Kubicki JD, Flynn GW, Heinz TF, Eisenthal KB. Second-harmonic generation and theoretical studies of protonation at the water/α-TiO2 (110) interface. Chem Phys Lett 2005; 411(4–6): 399-403.

Fitts JP, Shang X, Flynn GW, Heinz TF, Eisenthal KB. Electrostatic surface charge at aqueous/α-Al2O3 single-crystal interfaces as probed by optical second-harmonic generation. J Phys Chem B 2005; 109(16): 7981-7986.

Flörsheimer M. Second-harmonic microscopy – new tool for the remote sensing of interfaces. Phys Stat Sol (A) 1999; 173(1): 15-27.

Fordyce AJ, Bullock WJ, Timson AJ, Haslam S, Spencer-Smith RD, Alexander A, Frey JG. The temperature dependence of surface second-harmonic generation from the air-water interface. Mol Phys 2001; 99(8): 677-687.

Franken PA, Hill AE, Peters CW, Weinreich G. Generation of optical harmonics. Phys Rev Lett 1961; 7(4): 118-119.

Freund I, Deutsch M. Second-harmonic microscopy of biological tissue. Opt Lett 1986; 11(2): 94-96.

Frye JM, Schauer MW, Pellin MJ, Gruen DM, Melendres CA. Nickel passivation in acidic chloride solution using optical second harmonic generation. Chem Mater 1990; 2(3): 245-48.

Gaarenstroom SW. Principal component analysis of auger line shapes at solid – solid interfaces. Appl Surf Sci 1981; 7(1–2): 7-18.

Geiger FM. Second harmonic generation, sum frequency generation, and χ(3) : dissecting environmental interfaces with a nonlinear optical Swiss army knife. Annu Rev Phys Chem 2009; 60(1): 61-83.

Georgiadis R, Richmond GL. Wavelength-dependent second harmonic generation from silver(111) in solution. J Phys Chem 1991; 95(7): 2895-2899.

Goldacker T, Abetz V, Stadler R, Erukhimovich I, Leibler L. Non-centrosymmetric superlattices in block copolymer blends. Nature 1999; 398(6723): 137-139.

Grubb SG, Kim MW, Rasing T, Shen YR. Orientation of molecular monolayers at the liquid-liquid interface as studied by optical second harmonic generation. Langmuir 1988; 4(2): 452-454.

Gürdal E, Horneber A, Shaqqura N, Meixner AJ, Kern DP, Zhang D, Fleischer M. Enhancement of the second harmonic signal of nonlinear crystals by self-assembled gold nanoparticles. J Phys Chem 2020; 152(10): 104711.

Guyot-Sionnest P, Chen W, Shen YR. General considerations on optical second-harmonic generation from surfaces and interfaces. Phys Rev B 1986; 33(12): 8254-8263.

Halasyamani PS, Rondinelli JM. The must-have and nice-to-have experimental and computational requirements for functional frequency doubling deep-UV crystals. Nat Commun 2018; 9(1): 2972.

Hamal P, Nguyenhuu H, Don VS, Kumal RR, Kumar R, McCarley RL, Haber LH. Molecular adsorption and transport at liposome surfaces studied by molecular dynamics simulations and second harmonic generation spectroscopy. J Phys Chem B 2019; 123(36): 7722-7730.

Hamilton JC, Anderson RJM. The effect of adsorbed CO on azimuthally resolved optical second harmonic generation from Ni(111). Chem Phys Lett 1988; 151(4–5): 455-460.

Hamilton JC, Williams LR, Anderson RJM. Electronic resonances in azimuthally resolved optical second-harmonic generation from Pd(111) with hydrogen and carbon monoxide. Chem Phys Lett 1990; 167(6): 507-512.

He X, Hu D, Yang G, Adamietz F, Rodriguez V, Dussauze M, Fargues A, Fargin E, Cardinal T. Microstructured SHG patterns on Sm2O3-doped borophosphate niobium glasses by laser-induced thermal poling. Ceram Int 2021; 47(7): 10123-10129.

Heinz T. Nonlinear optics of surfaces and adsorbates. Berkeley: University of California Berkeley. 1982.

Heinz T. Second-order nonlinear optical effects at surfaces and interfaces. In: Ponath HE, Stegeman GI, eds. Nonlinear Surface Electromagnetic Phenomena. 1st ed. Amsterdam: North-Holland. 1991: 353-416.

Hicks JM, Kemnitz K, Eisenthal KB, Heinz TF. Studies of liquid surfaces by second harmonic generation. J Phys Chem 1986; 90(4): 560-562.

Higgins DA, Corn RM. Second harmonic generation studies of adsorption at a liquid-liquid electrochemical interface. J Phys Chem 1993; 97(2): 489-493.

Himpsel FJ, Heinz TF, McLean AB, Palange E, Burstein E. Two-dimensional energy bands at the CaF2/Si(111) interface. J Vac Sci Technol 1989; 7(4): 879-881.

Hristu R, Stanciu SG, Dumitru A, Eftimie LG, Paun B, Tranca DE, Gheorghita P, Costache M, Stanciu GA. PSHG-TISS: a collection of polarization-resolved second harmonic generation microscopy images of fixed tissues. Sci Data 2022; 9(1): 376.

Huang JY, Lewis A, Loew L. Nonlinear optical properties of potential sensitive styryl dyes. Biophys J 1988; 53(5): 665-670.

Huttunen MJ, Virkki M, Erkintalo M, Vuorimaa E, Efimov A, Lemmetyinen H, Kauranen M. Absolute probe of surface chirality based on focused circularly polarized light. J Phys Chem Lett 2010; 1(12): 1826-1829.

Johnson PB, Karvounis A, Singh HJ, Brereton CJ, Bourdakos KN, Lunn K, Roberts JJW, Davies DE, Muskens OL, Jones MG, Mahajan S. Superresolved polarization-enhanced second-harmonic generation for direct imaging of nanoscale changes in collagen architecture. Optica 2021; 8(5): 674-685.

Kaneshiro J, Okada Y, Shima T, Tsujii M, Imada K, Ichimura T, Watanabe TM. Second harmonic generation polarization microscopy as a tool for protein structure analysis. Biophys Physicobiol 2019; 16(0): 147-157.

Kang L, Lin Z. Second harmonic generation of MoSi2N4-type layers. Phys Rev B 2021; 103(19): 195404.

Karunendiran A, Mirsanaye K, Stewart BA, Barzda V. 2022. Second harmonic generation properties in chiral sarcomeres of Drosophila larval muscles. Front Phys 2022; 10: 758509.

Kleinman DA. Theory of second harmonic generation of light. Phys Rev 1962; 128(4): 1761-1775.

Klenerman D, Hodge J, Joseph M. Second harmonic generation at surfaces applied to corrosion inhibition. Corros Sci 1994; 36(2): 301-313.

Konek CT, Musorrafiti MJ, Voges AB, Geiger FM. Tracking the interaction of transition metal ions with environmental interfaces using second harmonic generation. In: Barnett M, Kent D, eds. Adsorption of Metals by Geomedia II. New York: Elsevier. 2008: 95-124.

Kott KL, Higgins DA, McMahon RJ, Corn RM. Observation of photoinduced electron transfer at a liquid-liquid interface by optical second harmonic generation. J Am Chem Soc 1993; 115(12): 5342-5343.

Krasnok A, Tymchenko M, Alù A. Nonlinear metasurfaces: a paradigm shift in nonlinear optics. Mater Today 2018; 21(1): 8-21.

Kriech MA, Conboy JC. 2004. Counterpropagating second-harmonic generation: a new technique for the investigation of molecular chirality at surfaces. J Opt Soc Am B 2004; 21(5): 1013-1022.

Kriech MA, Conboy JC. Imaging chirality with surface second harmonic generation microscopy. J Am Chem Soc 2005; 127(9): 2834-2835.

Kurimura S, Harada M, Muramatsu K, Ueda M, Adachi M, Yamada T, Ueno T. Quartz revisits nonlinear optics: twinned crystal for quasi-phase matching. Opt Mater Express 2011; 1(7): 1367-1375.

Lam RK, Raj SL, Pascal TA, Pemmaraju CD, Foglia L, Simoncig A, Fabris N, Miotti P, Hull CJ, Rizzuto AM, Smith JW, Mincigrucci R, Masciovecchio C, Gessini A, Allaria E, De Ninno G, Diviacco B, Roussel E, Spampinati S, Penco G, Di Mitri S, Trovò M, Danailov M, Christensen ST, Sokaras D, Weng TC, Coreno M, Poletto L, Drisdell WS, Prendergast D, Giannessi L, Principi E, Nordlund D, Saykally RJ, Schwartz CP. Soft x-ray second harmonic generation as an interfacial probe. Phys Rev Lett 2018; 120(2): 023901.

Lambert AG, Davies PB, Neivandt DJ. Implementing the theory of sum frequency generation vibrational spectroscopy: a tutorial review. Appl Spectrosc Rev 2005; 40(2): 103-145.

Lantz JM, Corn RM. 1994. Time-resolved optical second harmonic generation measurements of picosecond band flattening processes at single crystal TiO2 electrodes. J Phys Chem 1994; 98(38): 9387-9390.

Lee S, Makan S, Holl MMB, McFeely FR. Synthetic control of solid/solid interfaces: analysis of three new silicon/silicon oxide interfaces by soft x-ray photoemission. J Am Chem Soc 1994; 116(26): 11819-11826.

Li J, Hu G, Shi L, He N, Li D, Shang Q, Zhang Q, Fu H, Zhou L, Xiong W, Guan J, Wang J, He S, Chen L. Full-color enhanced second harmonic generation using rainbow trapping in ultrathin hyperbolic metamaterials. Nat Commun 2021; 12(1): 6425.

Lin L, Zhang Z, Guo Y, Liu M. 2018. Fabrication of supramolecular chirality from achiral molecules at the liquid/liquid interface studied by second harmonic generation. Langmuir 2018; 34(1): 139-146.

Liu J, Cho I, Cui Y, Irudayaraj J. Second harmonic super-resolution microscopy for quantification of MRNA at single copy sensitivity. ACS Nano 2014; 8(12): 12418-12427.

Liu Y, Yan ECY, Zhao X, Eisenthal KB. Surface potential of charged liposomes determined by second harmonic generation. Langmuir 2008; 24(19): 11322.

Lu K, Luo M, Gao W, Wang QJ, Sun H, Nam D. Strong second-harmonic generation by sublattice polarization in non-uniformly strained monolayer graphene. Nat Commun 2023; 14(1): 2580.

Lukina MM, Dudenkova VV, Shimolina LE, Snopova LB, Zagaynova EV, Shirmanova MV. In vivo metabolic and SHG imaging for monitoring of tumor response to chemotherapy. Cytometry A 2019; 95(1): 47-55.

Lüpke G. Characterization of semiconductor interfaces by second-harmonic generation. Surf Sci Rep 1999; 35(3-4): 75-161.

Ma E, Geiger FM. Divalent ion specific outcomes on stern layer structure and total surface potential at the silica:water interface. J Phys Chem A 2021; 125(46): 10079-10088.

Ma E, Kim J, Chang H, Ohno PE, Jodts RJ, Miller TF, Geiger FM. Stern and diffuse layer interactions during ionic strength cycling. J Phys Chem C 2021; 125(32): 18002-18014.

Ma E, Ohno PE, Kim J, Liu Y, Lozier EH, Miller TF, Wang H, Geiger FM. A new imaginary term in the second-order nonlinear susceptibility from charged interfaces. J Phys Chem Lett 2021; 12(24): 5649-5659.

Mahoney CM, Fahey AJ, Steffens KL, Benner BA, Lareau RT. Characterization of composition C4 explosives using time-of-flight secondary ion mass spectrometry and x-ray photoelectron spectroscopy. Anal Chem 2010; 82(17): 7237-7248.

Maiman TH. Stimulated optical radiation in ruby. Nature 1960; 187(4736): 493-494.

Manzeli S, Ovchinnikov D, Pasquier D, Yazyev OV, Kis A. 2D transition metal dichalcogenides. Nat Rev Mater 2017; 2(8): 17033.

Marrucci L, Paparo D, Cerrone G, de Lisio C, Santamato E, Solimeno S, Ardizzone S, Quagliotto P. Probing interfacial properties by optical second-harmonic generation. Opt Lasers Eng 2002; 37(5): 601-610.

Martinez IS, Peterson MD, Ebben CJ, Hayes PL, Artaxo P, Martin ST, Geiger FM. On molecular chirality within naturally occurring secondary organic aerosol particles from the central amazon basin. Phys Chem Chem Phys 2011; 13(26): 12114-12122.

Martin-Gassin G, Gassin PM, Couston L, Diat O, Benichou E, Brevet PF. 2011. Second harmonic generation monitoring of nitric acid extraction by a monoamide at the water–dodecane interface. Phys Chem Chem Phys 2011; 13(43): 19580-19586.

McGeachy AC, Caudill ER, Liang D, Cui Q, Pedersen JA, Geiger FM. Counting charges on membrane-bound peptides. Chem Sci 2018; 9(18): 4285-4298.

Mifflin AL, Konek CT, Geiger FM. Tracking oxytetracyline mobility across environmental interfaces by second harmonic generation. J Phys Chem B 2006; 110(45): 22577-22585.

Mifflin AL, Musorrafiti MJ, Konek CT, Geiger FM. Second harmonic generation phase measurements of Cr(VI) at a buried interface. J Phys Chem B 2005; 109(51): 24386-24390.

Mirsanaye K, Castaño LU, Kamaliddin Y, Golaraei A, Augulis R, Kontenis L, Done SJ, Žurauskas E, Stambolic V, Wilson BC, Barzda V. Machine learning-enabled cancer diagnostics with widefield polarimetric second-harmonic generation microscopy. Sci Rep 2022; 12(1): 10290.

Mostaco-Guidolin LB, Loube J, Barlow A, Osei ET, Vasilescu DM, Hsieh A, Fouadi M, Young C, Scott AL, Mitzner W, Hackett TL. Second harmonic generation imaging of collagen scaffolds within the alveolar ducts of healthy and emphysematous mouse lungs. Histochem Cell Biol 2021; 155(2): 279-289.

Murakami Y, Masaki M, Miyazaki S, Oketani R, Hayashi Y, Yanagisawa M, Honjoh S, Kano H. Spectroscopic second and third harmonic generation microscopy using a femtosecond laser source in the third near-infrared (NIR-III) optical window. Biomed Opt Express 2022; 13(2): 694-708.

Myers D. Surface, Interfaces, and Colloids: Principles and Applications. 2nd ed. New York:John Wiley & Sons, Inc. 1999

Nappa, J, Revillod G, Russier-Antoine I, Benichou E, Jonin C, Brevet PF. 2005. Electric dipole origin of the second harmonic generation of small metallic particles. Phys Rev B 2005; 71(16): 165407.

Nemet BA, Nikolenko V, Yuste R. 2004. Second harmonic imaging of membrane potential of neurons with retinal. J Biomed Opt 2004; 9(5): 873-881.

New G. Introduction to Nonlinear Optics. Cambridge:Cambridge University Press. 2011.

Nguyen KT, Le Clair SV, Ye S, Chen Z. Molecular interactions between magainin 2 and model membranes in situ. J Phys Chem B 2009; 113(36): 12358-12363.

Nguyen TT, Conboy JC. High-throughput screening of drug–lipid membrane interactions via counter-propagating second harmonic generation imaging. Anal Chem 2011; 83(15): 5979-5988.

Ong S, Zhao X, Eisenthal KB. Polarization of water molecules at a charged interface: second harmonic studies of the silica/water interface. Chem Phys Lett 1992; 191(3-4): 327-335.

Pantazis P, Maloney J, Wu D, Fraser SE. Second harmonic generating (SHG) nanoprobes for in vivo imaging. Proc Natl Acad Sci 2010; 107(33): 14535-14540.

Perkampus H. UV-VIS Spectroscopy and Its Applications. Springer Lab Manuals. 1992.

Peterson MD, Hayes PL, Martinez IS, Cass LC, Achtyl JL, Weiss EA, Geiger FM. 2011. Second harmonic generation imaging with a KHz amplifier. Opt Mater Express 2011; 1(1): 57-66.

Petralli-Mallow TP, Plant AL, Lewis ML, Hicks JM. Cytochrome C at model membrane surfaces: exploration via second harmonic generation-circular dichroism and surface-enhanced resonance Raman spectroscopy. Langmuir 2000; 16(14): 5960-5966.

Petralli-Mallow T, Wong TM, Byers JD, Yee HI, Hicks JM. 1993. Circular dichroism spectroscopy at interfaces: a surface second harmonic generation study. J Phys Chem 1993; 97(7): 1383-1388.

Pham TT, Hong EM, Moy WJ, Zhao J, Hu AC, Barnes CH, Borden PA, Sivoraphonh R, Krasieva TB, Lee LH, Heidari AE, Kim EH, Nam SH, Jia W, Mo J, Kim S, Hill MG, Wong BJF. The biophysical effects of localized electrochemical therapy on porcine skin. J Dermatol Sci 2020; 97(3): 179-186.

Poirier G, Dussauze M, Rodriguez V, Adamietz F, Karam L, Cardinal T, Fargin E. Second harmonic generation in sodium tantalum germanate glasses by thermal poling. J Phys Chem C 2019; 123(43): 26528-26535.

Purnell GE, Walker RA. 2019. Surface solvation and hindered isomerization at the water/silica interface explored with second harmonic generation. J Chem Phys 2019; 150(19): 194701.

Qi S, Ge F, Han X, Cheng P, Shi R, Liu C, Zheng Y, Xin M, Xu J. 0D chiral hybrid indium(III) halides for second harmonic generation. Dalton Trans 2022; 51(22): 8593-8599.

Rao Y, Tao Y, Wang H. Quantitative analysis of orientational order in the molecular monolayer by surface second harmonic generation. J Chem Phys 2003; 119(10): 5226-5236.

Rasing T. 1994. Studies of buried interfaces by optical second-harmonic generation. Appl Phys A 1994; 59(5): 531-536.

Rasing T, Shen YR, Kim MW, Grubb S. Observation of molecular reorientation at a two-dimensional-liquid phase transition. Phys Rev Lett 1985; 55(26): 2903-2906.

Rasing T, Shen YR, Kim MW, Valint P, Bock J. Orientation of surfactant molecules at a liquid-air interface measured by optical second-harmonic generation. Phys Rev A 1985; 31(1): 537-539.

Revillod G, Duboisset J, Russier-Antoine I, Benichou E, Jonin C, Brevet P. Second harmonic scattering of molecular aggregates. Symmetry 2021; 13(2): 206.

Richmond GL, Rojhantalab HM, Robinson JM, Shannon VL. Experiments on optical second-harmonic generation as a surface probe of electrodes. J Opt Soc Am B 1987; 4(2): 228-236.

Salafsky JS, Eisenthal KB. Second harmonic spectroscopy: detection and orientation of molecules at a biomembrane interface. Chem Phys Lett 2000; 319(5-6): 435-439.

Saslow Gomez SA, Jordan DS, Troiano JM, Geiger FM. Uranyl adsorption at the muscovite (mica)/water interface studied by second harmonic generation. Environ Sci Technol 2012; 46(20): 11154-11161.

Schauer MW, Pellin MJ, Gruen DM. Angularly resolved second harmonic generation study of the air formed oxide on iron. Chem Mater; 1989; 1(1): 101-105.

Schultz KA, Suni II, Seebauer EG. Microscopy of adsorbates by surface second-harmonic generation. J Opt Soc Am B 1993; 10(3): 546-550.

Schulze M, Utecht M, Moldt T, Przyrembel D, Gahl C, Weinelt M, Saalfrank P, Tegeder P. Nonlinear optical response of photochromic azobenzene-functionalized self-assembled monolayers. Phys Chem Chem Phys 2015; 17(27): 18079-18086.

Seyler KL, de la Torre A, Porter Z, Zoghlin E, Polski R, Nguyen M, Nadj-Perge S, Wilson SD, Hsieh D. Spin-orbit-enhanced magnetic surface second-harmonic generation in Sr2IrO4. Phys Rev B 2020; 102(20): 201113.

Shannon VL, Koos DA, Richmond GL. Second harmonic generation for in situ analysis of electrode surface structure. Appl Opt 1987; 26(17): 3579-3583.

Shcherbakov MR, Zhang H, Tripepi M, Sartorello G, Talisa N, AlShafey A, Fan Z, Twardowski J, Krivitsky LA, Kuznetsov AI, Chowdhury E, Shvets G. Generation of even and odd high harmonics in resonant metasurfaces using single and multiple ultra-intense laser pulses. Nat Commun 2021; 12(1): 4185.

Shen YR. Surface properties probed by second-harmonic and sum-frequency generation. Nature 1989; 337(6207): 519-525.

Simpson GJ. Molecular origins of the remarkable chiral sensitivity of second-order nonlinear optics. Chem Phys Chem 2004; 5(9): 1301-1310.

Simpson GJ, Rowlen KL. An SHG magic angle: dependence of second harmonic generation orientation measurements on the width of the orientation distribution. J Am Chem Soc 1999; 121 (11): 2635-2636.

Sipe J, Moss D, van Driel H. Phenomenological theory of optical second- and third-harmonic generation from cubic centrosymmetric crystals. Phys Rev B 1987; 35(3): 1129-1141.

Sitzmann EV, Eisenthal KB. Picosecond dynamics of a chemical reaction at the air-water interface studied by surface second harmonic generation. J Phys Chem 1988; 92(16): 4579-4580.

Smolyaninov II, Liang HY, Lee CH, Davis CC. Local crystal analysis using near-field optical second harmonic microscopy: application to thin ferroelectric films. J Appl Phys 2001; 89(1): 206-211.

Somorjai GA. Introduction to Surface Chemistry and Catalysis. New Jersey: Wiley-Interscience. 1994.

Somorjai GA, Li Y. Introduction to Surface Chemistry and Catalysis. 2nd ed. Hoboken: John Wiley & Sons, Inc. 2010.

Sonay AY, Kalyviotis K, Yaganoglu S, Unsal A, Konantz M, Teulon C, Lieberwirth I, Sieber S, Jiang S, Behzadi S, Crespy D, Landfester K, Roke S, Lengerke C, Pantazis P. Biodegradable harmonophores for targeted high-resolution in vivo tumor imaging. ACS Nano 2021; 15(3): 4144-4154.

Srivastava A, Eisenthal KB. Kinetics of molecular transport across a liposome bilayer. Chem Phys Lett 1998; 292(3): 345-351.

Stokes GY, Conboy JC. Measuring selective estrogen receptor modulator (SERM)–membrane interactions with second harmonic generation. J Am Chem Soc 2014; 136(4): 1409-1417.

Tarun OB, Eremchev MY, Roke S. Interaction of oil and lipids in freestanding lipid bilayer membranes studied with label-free high-throughput wide-field second-harmonic microscopy. Langmuir 2018; 34(38): 11305-11310.

Tarun OB, Hannesschläger C, Pohl P, Roke S. Label-free and charge-sensitive dynamic imaging of lipid membrane hydration on millisecond time scales. Proc Natl Acad Sci 2018; 115(16): 4081-4086.

Tokman M, Bodrov SB, Sergeev YA, Korytin AI, Oladyshkin I, Wang Y, Belyanin A, Stepanov AN. Second harmonic generation in graphene dressed by a strong terahertz field. Phys Rev B 2019; 99(15): 155411.

Tom HWK, Mate CM, Zhu XD, Crowell JE, Heinz TF, Somorjai GA, Shen YR. Surface studies by optical second-harmonic generation: the adsorption of O2, CO, and sodium on the Rh(111) surface. Phys Rev Lett 1984; 52(5): 348-351.

Tverjanovich A, Borisov EN, Kassem M, Masselin P, Fontanari D, Bychkov E. Intrinsic second-order nonlinearity in chalcogenide glasses containing HgI2. J Am Ceram Soc 2020; 103(5): 3070-3075.

Uchida T, Yamaguchi A, Ina T, Teramae N. Observation of molecular association at liquid/liquid and solid/liquid interfaces by second harmonic generation spectroscopy. J Phys Chem B 2000; 104(51): 12091-12094.

Valev VK, Zheng X, Biris CG, Silhanek AV, Volskiy V, De Clercq B, Aktsipetrov OA, Ameloot M, Panoiu NC, Vandenbosch AE, Moshchalkov VV. The origin of second harmonic generation hotspots in chiral optical metamaterials. Opt Mater Express 2011; 1(1): 36-45.

Van Huizen L, Kramer T, Seinstra D, Radonic T, Dickhoff C, Daniels H, Bahce I, Bonta P, Annema J, Groot M. Instant on-site histological analysis of fresh lung tumor tissue using third and second harmonic generation microscopy. Eur Respir J 2020; 56: 1640.

Vanbel MK, Su C, Locquet J, Verbiest T. Electric-field-induced second-harmonic generation demonstrates different interface properties of molecular beam epitaxy grown MgO on Si. J Phys Chem C 2014; 118(4): 1919-1924.

Vianna PG, Almeida ADS, Gerosa RM, Bahamon DA, de Matos CJS. Second-harmonic generation enhancement in monolayer transition-metal dichalcogenides by using an epsilon-near-zero substrate. Nanoscale Adv 2021; 3(1): 272-278.

Violakis G, Tsafas V, Filippidis G, Pissadakis S. Electrically poled, MNA-microstructured optical fibers for second harmonic generation. IEEE J Sel Top Quantum Electron 2020; 26(4): 1-8.

Wang CC. Second-harmonic generation of light at the boundary of an isotropic medium. Phys Rev 1969; 178(3): 1457-1460.

Wang H, Yan ECY, Borguet E, Eisenthal KB. Second harmonic generation from the surface of centrosymmetric particles in bulk solution. Chem Phys Lett 1996; 259(1-2): 15-20.

Wang H, Borguet E, Eisenthal KB. Polarity of liquid interfaces by second harmonic generation spectroscopy. J Phys Chem A 1997; 101(4): 713-718.

Wang H, Gan W, Lu R, Rao Y, Wu B. Quantitative spectral and orientational analysis in surface sum frequency generation vibrational spectroscopy (SFG-VS). Int Rev Phys Chem 2005; 24(2): 191-256.

Wang H, Mao Y, Kislyakov I, Dong N. Anisotropic Raman scattering and intense broadband second-harmonic generation in tellurium nanosheets. Opt Lett 2021; 46(8): 1812-1815.

Wang R, Wang F, Long J, Tao Y, Zhou L, Fu H, Liu Y, Jiao B, Deng L, Xiong W. Polarized second-harmonic generation optical microscopy for laser-directed assembly of ZnO nanowires. Opt Lett 2019; 44(17): 4291-4294.

Wang Y, Shi P, Xu K, He L, Meng X, Ye Q. Dielectric switching, SHG response and Pd(II) adsorption of a multifunctional phase-transition complex. Inorg Chem Front 2021; 8(22): 4858-4863.

Wilhelm MJ, Dai H. Nonlinear light scattering from buried interfaces: fundamentals and applications. In: Berman MR, Young L, Dai H, eds. Emerging Trends in Chemical Applications of Lasers. Washington: ACS Publications. 2021:173–98.

Wu W, Fang H, Yang F, Chen S, Zhu X, Yuan Q, Gan W. Understanding the different steps of surfactant adsorption at the oil–water interface with second harmonic generation. J Phys Chem C 2016; 120(12): 6515-6523.

Wu W, Liu X, Chen S, Yuan Q, Gan W. Particle adsorption at the oil–water interface studied with second harmonic generation. Soft Matter 2019; 15(38): 7672-7677.

Xu P, Huang A, Suntivich J. Phase-sensitive second-harmonic generation of electrochemical interfaces. J Phys Chem Lett 2020; 11(19): 8216-8221.

Xue M, Zhang L, Liu M, Bai Y, Guo Y, Zhang Z. Metal ion mediation of interfacial chiral supramolecular formation of amphiphilic Schiff bases studied by in situ second harmonic generation. J Phys Chem B 2020; 124(37): 8179-8187.

Yamin K, Assa M, Matityahu A, Onn I. Analyzing chromosome condensation in yeast by second-harmonic generation microscopy. Curr Genet 2020; 66(2): 437-443.

Yan ECY, Liu Y, Eisenthal KB. In situ studies of molecular transfer between microparticles by second-harmonic generation. J Phys Chem B 2001; 105(36): 8531-8537.

Yan ECY, Liu Y, Eisenthal KB. New method for determination of surface potential of microscopic particles by second harmonic generation. J Phys Chem B 1998; 102(33): 6331-6336.

Yan ECY, Eisenthal KB. 2000. Effect of cholesterol on molecular transport of organic cations across liposome bilayers probed by second harmonic generation. Biophys J 2000; 79(2): 898-903.

Yang F, Song W, Meng F, Luo F, Lou S, Lin S, Gong Z, Cao J, Barnard ES, Chan E, Yang L, Yao J. Tunable second harmonic generation in twisted bilayer graphene. Matter 2020; 3(4): 1361-1376.

Yao K, Finney NR, Zhang J, Moore SL, Xian L, Tancogne-Dejean N, Liu F, Ardelean J, Xu X, Halbertal D, Watanabe K, Taniguchi T, Ochoa H, Asenjo-Garcia A, Zhu X, Basov DN, Rubio A, Dean C, Hone J, Schuck PJ. Enhanced tunable second harmonic generation from twistable interfaces and vertical superlattices in boron nitride homostructures. Sci Adv 2021; 7(10).

Ying J, Liu F, Ho PP, Alfano RR. Nondestructive evaluation of incipient corrosion in a metal beneath paint by second-harmonic tomography. Opt Lett 2000; 25(16): 1189-1191.

Young VY, Hoflund GB. Surface analysis using ion scattering spectroscopy: effect of resolution and intensity measure on surface atom density ratios. Anal Chem 1988; 60(3): 269-274.

Zhang C, Zeng G, Zhang R, Tang Y, Liu Q, Jiang T. Tunable nonlinear optical responses of few-layer graphene through lithium intercalation. Nanophotonics 2021; 10(10): 2661-2669.

Zhang J, Zhao W, Yu P, Yang G, Liu Z. Second harmonic generation in 2D layered materials. 2d Mater 2020; 7(4): 042002.

Zhang Y, Grady NK, Ayala-Orozco C, Halas NJ. Three-dimensional nanostructures as highly efficient generators of second harmonic light. Nano Lett 2011; 11(12): 5519-5523.

Zheng M, Fujita K, Chen W, Duan X, Kawata S. Two-photon excited fluorescence and second-harmonic generation of the DAST organic nanocrystals. J Phys Chem C 2011; 115(18): 8988-8993.

Zhou H, Hahn D, Wong GK, Roscoe SB, Marks TJ. Anisotropic second-harmonic generation from chromophoric self-assembled monolayers upon oxide overlayers of Si(111) surfaces. J Opt Soc Am B 1997; 14(2): 391-395.

Zhu C, Zhang Z, Qin J, Wang Z, Wang C, Miao P, Liu Y, Huang P, Zhang Y, Xu K, Zhen L, Chai Y, Xu C. Two-dimensional semiconducting SnP2Se6 with giant second-harmonic-generation for monolithic on-chip electronic-photonic integration. Nat Commun 2023; 14(1): 2521.

Zhu XD, Daum W, Xiao X, Chin R, Shen YR. Coverage dependence of surface optical second-harmonic generation from CO/Ni(110): investigation with a nonlinear-interference technique. Phys Rev B 1991; 43(14): 11571-11580.

Zhu XD, Rasing T, Shen YR. Surface diffusion of Co on Ni(111) studied by diffraction of optical second-harmonic generation off a monolayer grating. Phys Rev Lett 1988; 61(25): 2883-2885.

Zhuang Z, Qu H, Yang W, Liu J, Wang F, Liu Y, Ding J, Shi J. Comparing hepatic steatosis distribution patterns between non-alcoholic fatty liver disease and fatty liver disease with chronic hepatitis B by second-harmonic generation/two-photon excited fluorescence method. Ann Hepatol 2020; 19(3): 313-319.